Finding Lottery Tickets in Vision Models via Data-driven Spectral Foresight Pruning

Virtual Element simulation of two-phase flow of immiscible fluids in Discrete Fracture Networks

S. Berrone*, M. Busetto*, F. Vicini*

Abstract

In this paper we propose a primal C^0-conforming virtual element discretization for the simulation of the two-phase flow of immiscible fluids in poro-fractured media modelled by means of a Discrete Fracture Network (DFN). The fractures are assumed to be made of the same isotropic rock type and to have the same width. The flexibility of the Virtual Element Method (VEM) in handling general polygonal elements allows to obtain a global conformity of the DFN mesh while preserving a fracture-independent meshing approach. The effectiveness and the robustness of the proposed numerical method are tested on DFN configurations of increasing complexity and characterized by challenging mesh geometry.

Keywords: Virtual element method, Two-phase immiscible flow, Porous media, Discrete fracture networks, Polygonal mesh

AMS: 65M50, 65M60, 76S05, 76T99

1 Introduction

Natural rocks involve intrinsic discontinuities on different scales and of different geometries called fractures. The presence of fractures strongly influences and complicates flow and transport phenomena within the medium. Indeed, they can act either as channels or as barriers for the flow of the fluids [1]. Understanding the behaviour of fluids flow and, in particular, of two-phase flow of immiscible fluids, in fractured media, is of fundamental importance in various geological engineering applications like enhanced oil recovery in fractured reservoir, geological carbon sequestration and nuclear waste management in subsurface. However, the simulation of this underground phenomenon is still very challenging due to both the complexity of the computational domain and the stochasticity of the subsoil data [2, 3].

Different models for the representation of multiphase flow in fractured media exist [4]. On the one hand, there are the continuum models and on the other hand, the discrete fracture models. In the former the fractures are included in the model through homogenization [5], whereas in the latter they are included individually. Discrete fracture models include both more refined models that take into account the exchange between the fractures and the surrounding medium, and simplified models that consider the flow outside the fractures negligible [6].

In this work, we consider the Discrete Fracture Network (DFN) model; in a DFN the porous matrix is neglected, thus the flow of fractures do not communicate with the surrounding medium. This approach provides acceptable results when the permeability of the surrounding medium is much lower than the one of the fractures. Each fracture is dimensionally reduced to a planar object in the three-dimensional space and coupling conditions are imposed at the intersections between the fractures, named in what follows as traces [7]. The positions and the orientations of the fractures are randomly generated according to different probability distribution laws. With respect to the traditional DFN, in our model, we introduce an additional assumption. Indeed,

*Department of Applied Mathematics, Politecnico di Torino, Italy (stefano.berrone@polito.it, martina.busetto@polito.it, fabio.vicini@polito.it).

we require that all the fractures have the same width and they are made of the same isotropic rock type.

Despite its simplicity, the DFN model still retains complexity due to the presence of randomly generated fractures that can lead to complex geometrical configurations involving small angles, almost parallel fractures and traces characterized by different lengths. Consequently, numerical techniques able to handle complicated domains are needed. Standard approaches involve either the use of conforming meshes at the interfaces combined with standard finite element or finite volume methods [8, 9, 10] or the use of non-conforming meshes at the interfaces combined with XFEM based approximations or unconventional domain decomposition schemes [11, 12, 13, 14, 15]. Obtaining a good globally conforming mesh can be very computationally demanding. Since the need to simplify the process of construction of a locally and globally conforming mesh, recently, methods based on general polygonal tessellations of the domain such as Hybrid High Order (HHO) methods [16], Mimetic Finite Difference (MFD) methods [17] and Virtual Element Methods (VEM) [18, 19, 20, 21] are gaining considerable interest.

The study of numerical methods for discrete fracture models for single phase flow in poro-fractured media is well established in literature [3, 7, 8, 22, 23, 24]. Conversely, the study of numerical discretization for discrete fracture models for two-phase flow of immiscible fluids in porous media with fractures is still a very challenging issue. This is partially due to the difficulties in the treatment of the two-phase flow equations that consist of a system of coupled non-linear time-dependent partial differential equations [25, 26]. Examples of numerical discretizations can be found in [27, 28, 29, 30].

In [31] a VEM based approach has been proposed by the authors for the solution of the two-phase flow equations of immiscible fluids in porous media through an iterative IMplicit-Pressure-Implicit-Saturation method coupled with a primal C^0-conforming VEM. In this paper, we further extend this formulation to DFN.

In the present work, we propose for the first time a VEM approach for the simulation of two-phase flow of immiscible fluids in DFN assessing its potentialities in dealing with rather complicated geometrical configuration arising from the construction of globally conforming meshes. Starting from an originally regular globally non-conforming mesh, we construct a globally polygonal conforming mesh not crossing the traces. Then we exploit the robustness of the VEM in handling very general polygonal elements for the resolution of the two-phase flow problem. At the fracture-fracture intersections, we require continuity of the pressure of the non-wetting phase, balancing of the jumps of the normal components of the total Darcy velocity, continuity of the capillary pressure and balancing of the jumps of the normal components of the Darcy velocity of the wetting phase [32]. Since it is assumed that all the fractures of our DFN model have the same width and that they are all made of the same isotropic rock type, then the continuity of the capillary pressure implies the continuity of the saturation of the wetting phase on the traces.

The structure of this work is as follows. In Section 2, we introduce the model and its related equations. In Sections 3 and 4, we introduce the time and the space discretization of the problem following the same ideas introduced in [31]. In Section 5, we describe the construction of the global mesh and we present and discuss numerical results for DFN models of increasing complexity. Finally, in Section 6, we draw some conclusions.

2 The continuous problem

2.1 Single fracture

Let us consider a fracture $\Omega_f \subset \mathbb{R}^3$ and a time interval $\mathcal{I}_T := [0, T]$, with $T \in \mathbb{R}^+$. The fracture is supposed to be a porous medium; it is delimited above and below by two surfaces γ_1 and γ_2 and it has a width d that is very small compared to the size of Ω_f. In particular, we suppose that Ω_f is of the form $F \times (-\frac{d}{2}, \frac{d}{2})$, where F is the intersection of a plane with Ω_f so that each one of its elements can be written uniquely as $\boldsymbol{x} + \zeta \boldsymbol{n}$ with $\boldsymbol{x} \in F$, $\zeta \in (-\frac{d}{2}, \frac{d}{2})$ and $\boldsymbol{n}$ is a unit vector normal to F. Physically, the fracture Ω_f is contained in a porous medium $\Omega \subset \mathbb{R}^3$ that ideally can be divided into three non overlapping connected subdomains Ω_1, Ω_2 and Ω_f,

where the subdomains Ω_1 and Ω_2 represent the surrounding rock matrices. We denote by Γ_f the boundary of Ω_f excluded the two surfaces γ_1 and γ_2, i.e., $\partial\Omega_f := \gamma_1 \cup \gamma_2 \cup \Gamma_f$; moreover, we assume that $\partial\Omega_f \cap \partial\Omega_i = \gamma_i,\ i = 1, 2$, therefore, $\Gamma_f \subset \partial\Omega$.

We suppose that a two-phase flow of immiscible fluids takes place in the fracture Ω_f and we assume that the fracture does not communicate with the porous matrices Ω_1 and Ω_2. In the following, the index w will denote the wetting phase and the index n the non-wetting phase. Each one of the two phases ($\alpha = \{w, n\}$) is characterized by a pressure $p_\alpha = p_\alpha(\boldsymbol{x}, t)$ $[Pa]$, a saturation $S_\alpha = S_\alpha(\boldsymbol{x}, t) \in [0, 1]$ $[-]$ and a Darcy velocity $\boldsymbol{u}_\alpha = \boldsymbol{u}_\alpha(\boldsymbol{x}, t)$ $[m \cdot s^{-1}]$, i.e., volume of fluid flowing per unit time through a unit cross-sectional area normal to the direction of the flow. We assume both incompressibility of the fluids and time-independence of the porosity of the medium. The governing equations involve the volume conservation equation that because of the incompressibility of the two fluids is equivalent to the mass conservation equation, and the generalized Darcy's law

$$\begin{aligned}
&\Phi \frac{\partial S_\alpha}{\partial t} + \nabla \cdot \boldsymbol{u}_\alpha = q_\alpha, \quad \text{in} \quad \Omega_f \times \mathcal{I}_T, \\
&\boldsymbol{u}_\alpha = -\frac{k_{r\alpha}}{\mu_\alpha} \boldsymbol{K} (\nabla p_\alpha - \rho_\alpha \boldsymbol{g}), \quad \text{in} \quad \Omega_f \times \mathcal{I}_T,
\end{aligned}$$

plus the following coupling conditions on the saturations and on the pressures

$$\begin{aligned}
&S_w + S_n = 1, \quad \text{in} \quad \Omega_f \times \mathcal{I}_T, \\
&p_c = p_n - p_w, \quad \text{in} \quad \Omega_f \times \mathcal{I}_T.
\end{aligned}$$

The physical data appearing in the equations are: the porosity of the medium $\Phi = \Phi(\boldsymbol{x})$ $[-]$, the absolute permeability of the medium $\boldsymbol{K} = \boldsymbol{K}(\boldsymbol{x}) \in \mathbb{R}^{3\times3}$ $[m^2]$ that is a symmetric and positive definite tensor, the density for each phase ρ_α $[Kg{\cdot}m^{-3}]$, the scalar source/sink terms $q_\alpha = q_\alpha(\boldsymbol{x}, t)$ $[s^{-1}]$, the relative permeability for each phase $k_{r_\alpha} = k_{r_\alpha}(S_\alpha)$ $[-]$, the dynamic viscosity for each phase $\mu_\alpha = \mu_\alpha(\boldsymbol{x}, t)$ $[Pa \cdot s]$, the gravity acceleration vector $\boldsymbol{g} = (0, 0, -g) \in \mathbb{R}^3$ $[m \cdot s^{-2}]$ and the capillary pressure $p_c = p_c(S_\alpha)$ $[Pa]$.

The capillary pressure function p_c and the relative permeabilities k_{r_α} depend on the physical properties of the fluids and the rock, modelled as functions of the saturations S_α. In particular, we adopt the Brooks-Corey empirical model [33] that is typically applied to model physical systems in which the water represents the wetting phase and a liquid like oil represents the non-wetting phase. Firstly, we define the effective saturations $\bar{S}_w$ and $\bar{S}_n$ as

$$\bar{S}_w := \frac{S_w - S_{wr}}{1 - S_{wr} - S_{nr}}, \quad \bar{S}_n := \frac{S_n - S_{nr}}{1 - S_{wr} - S_{nr}},$$

where S_{wr} and S_{nr} are the residual saturations of the wetting and of the non-wetting phase, respectively. It can be noticed that $\bar{S}_w, \bar{S}_n \in [0, 1]$ and $\bar{S}_n + \bar{S}_w = 1$ in $\Omega_f \times \mathcal{I}_T$. Then, the capillary pressure-saturation function p_c and the relative permeabilities k_{rw} and k_{rn} are modelled as

$$p_c(S_w) = p_d \bar{S}_w^{-\frac{1}{\mu}}, \quad k_{rw}(S_w) = \bar{S}_w^{\frac{2+3\mu}{\mu}}, \quad k_{rn}(S_n) = \bar{S}_n^2 \Big(1 - (1 - \bar{S}_n)^{\frac{2+\mu}{\mu}}\Big).$$

where p_d is the entry pressure of the porous medium and μ is a parameter related to the size of the pore distribution.

In what follows, we adopt the pressure-saturation formulation of the two-phase flow of immiscible fluids in porous media [34]; in the considered formulation, the pressure of the non-wetting phase p_n and the saturation of the wetting phase S_w are the two primary variables.

We decompose the boundary Γ_f into disjoint sets $\Gamma_{f_{N_p}}$ and $\Gamma_{f_{D_p}}$, and into disjoint sets $\Gamma_{f_{N_S}}$ and $\Gamma_{f_{D_S}}$ such that

$$\Gamma_f := \Gamma_{f_{N_p}} \cup \Gamma_{f_{D_p}} = \Gamma_{f_{N_S}} \cup \Gamma_{f_{D_S}} \text{ with } \Gamma_{f_{N_p}} \cap \Gamma_{f_{D_p}} = \Gamma_{f_{N_S}} \cap \Gamma_{f_{D_S}} = \emptyset,$$

where $\Gamma_{f_{N_p}}$ and $\Gamma_{f_{D_p}}$ refer to the Neumann and Dirichlet boundary related to p_n, and $\Gamma_{f_{N_S}}$ and $\Gamma_{f_{D_S}}$ refer to the Neumann and Dirichlet boundary related to S_w. We denote by $\boldsymbol{n}_f$ the exterior pointing unit normal vector on $\partial\Omega_f$.

The problem of the two-phase flow of immiscible fluids can be formulated as

$$-\nabla\cdot\left\{\boldsymbol{K}\lambda\nabla p_n-\boldsymbol{K}\lambda_w\frac{dp_c}{dS_w}\nabla S_w-\boldsymbol{K}(\lambda_w\rho_w+\lambda_n\rho_n)\boldsymbol{g}\right\}=0\quad\text{in }\Omega_f\times\mathcal{I}_T, \tag{1a}$$

$$\Phi\frac{\partial S_w}{\partial t}+\nabla\cdot\left\{\boldsymbol{K}\lambda_w\frac{dp_c}{dS_w}\nabla S_w-\boldsymbol{K}\lambda_w\nabla p_n+\boldsymbol{K}\lambda_w\rho_w\boldsymbol{g}\right\}=0\quad\text{in }\Omega_f\times\mathcal{I}_T, \tag{1b}$$

$$\boldsymbol{u}\cdot\boldsymbol{n}_f=0\quad\text{on}\quad\gamma_i\times\mathcal{I}_T\quad i=1,2, \tag{1c}$$

$$\boldsymbol{u}_w\cdot\boldsymbol{n}_f=0\quad\text{on}\quad\gamma_i\times\mathcal{I}_T,\quad i=1,2, \tag{1d}$$

$$p_n=g_{_{D_p}}\quad\text{on}\quad\Gamma_{f_{D_p}}\times\mathcal{I}_T, \tag{1e}$$

$$\boldsymbol{u}\cdot\boldsymbol{n}_f=Q_{_{N_p}}\quad\text{on}\quad\Gamma_{f_{N_p}}\times\mathcal{I}_T, \tag{1f}$$

$$S_w=g_{_{D_S}}\quad\text{on}\quad\Gamma_{f_{D_S}}\times\mathcal{I}_T, \tag{1g}$$

$$\boldsymbol{u}_w\cdot\boldsymbol{n}_f=Q_{_{N_S}}\quad\text{on}\quad\Gamma_{f_{N_S}}\times\mathcal{I}_T, \tag{1h}$$

$$S_w=S_{w0}\quad\text{in}\quad\Omega_f,\ t=0, \tag{1i}$$

where $\lambda_\alpha:=k_{r_\alpha}/\mu_\alpha\ [Pa\cdot s]^{-1}$ is the mobility for each phase, $\lambda:=\lambda_n+\lambda_w\ [Pa\cdot s]^{-1}$ is the total mobility and $f_w:=\lambda_w/\lambda\ [-]$ is the fractional flow of the wetting phase.

The total velocity $\boldsymbol{u}:=\boldsymbol{u}_w+\boldsymbol{u}_n$ and the Darcy velocity $\boldsymbol{u}_w$ can be written as functions of p_n and S_w as follows

$$\boldsymbol{u}=-\boldsymbol{K}\lambda\nabla p_n+\mathbf{K}\lambda_w\nabla p_c+\boldsymbol{K}(\lambda_w\rho_w+\lambda_n\rho_n)\boldsymbol{g}, \tag{2a}$$

$$\boldsymbol{u}_w=f_w\boldsymbol{u}+\boldsymbol{K}f_w\lambda_n\nabla p_c+\boldsymbol{K}f_w\lambda_n(\rho_w-\rho_n)\boldsymbol{g}=\boldsymbol{K}\lambda_w\nabla p_c-\boldsymbol{K}\lambda_w\nabla p_n+\boldsymbol{K}\lambda_w\rho_w\boldsymbol{g}. \tag{2b}$$

Conditions (1c) and (1d) represent the impermeability of the rock matrices Ω_1 and Ω_2. For simplicity, we do not consider the presence of source/sink terms within the fracture, i.e. $q_\alpha=0$. Moreover, we point out that the derivative of the capillary pressure $\frac{dp_c}{dS_w}$ is negative; therefore, the term $\nabla\cdot\left(\boldsymbol{K}\lambda_w\frac{dp_c}{dS_w}\nabla S_w\right)$ is a stabilizing diffusive term.

We refer to Equation (1a) as the pressure equation, and to (1b) as the saturation equation; the former is elliptic with respect to p_n, whereas the latter is either a non-linear hyperbolic equation with respect to S_w if capillary pressure $p_c=0$ or a parabolic convection-diffusion equation if $p_c\neq 0$.

We notice that given (2a) and (2b), we can rewrite Equations (1a) and (1b) as

$$-\nabla\cdot\boldsymbol{u}=0\quad\text{in}\quad\Omega_f\times\mathcal{I}_T, \tag{3a}$$

$$\Phi\frac{\partial S_w}{\partial t}+\nabla\cdot\boldsymbol{u}_w=0\quad\text{in}\quad\Omega_f\times\mathcal{I}_T. \tag{3b}$$

Now, we consider a reduced model in which the fracture is represented by a bi-dimensional surface [32]; to this aim, we collapse the fracture domain Ω_f onto its central axis F. Consequently, the boundary $\Gamma_F:=\partial F$ of the new domain is obtained collapsing Γ_f on F as well; again the boundary consists of the union of disjoint sets $\Gamma_{F_{N_p}}$ and $\Gamma_{F_{D_p}}$, and disjoint sets $\Gamma_{F_{N_S}}$ and $\Gamma_{F_{D_S}}$. In this setting, we assume small variations of the physical quantities of interest along the normal direction of the fracture.

The equations on F are obtained integrating the equations of Ω_f over its transversal cross section in the direction normal to the fracture. To this aim, we introduce the tangential and the normal components to the fracture of the gradient operator $\nabla_{\boldsymbol{T}}$ and $\nabla_{\boldsymbol{N}}$. We assume that the absolute permeability $\boldsymbol{K}$ can be written as the sum of a normal component $\boldsymbol{K}_{\boldsymbol{N}}$ and a tangential component $\boldsymbol{K}_{\boldsymbol{T}}$ that are both invariant in the normal direction. Moreover, we decompose $\boldsymbol{u}$ and $\boldsymbol{u}_w$ into their normal and tangential components to the fracture, i.e., $\boldsymbol{u}=\boldsymbol{u}_{\boldsymbol{T}}+\boldsymbol{u}_{\boldsymbol{N}}$ with $\boldsymbol{u}_{\boldsymbol{N}}:=(\boldsymbol{u}\cdot\boldsymbol{n})\boldsymbol{n}$ and $\boldsymbol{u}_{\boldsymbol{T}}:=\boldsymbol{u}-\boldsymbol{u}_{\boldsymbol{N}}$, and $\boldsymbol{u}_w=\boldsymbol{u}_{w_{\boldsymbol{T}}}+\boldsymbol{u}_{w_{\boldsymbol{N}}}$ with $\boldsymbol{u}_{w_{\boldsymbol{N}}}:=(\boldsymbol{u}_w\cdot\boldsymbol{n})\boldsymbol{n}$ and $\boldsymbol{u}_{\boldsymbol{T}}:=\boldsymbol{u}_w-\boldsymbol{u}_{w_{\boldsymbol{N}}}$. We denote by $\boldsymbol{g}_{\boldsymbol{T}}$ the tangential component of the gravity vector.

In the reference system defined on the fracture Ω_f, Equation (3a) can be rewritten as

$$\nabla_{\boldsymbol{T}}\cdot\boldsymbol{u}+\nabla_{\boldsymbol{N}}\cdot\boldsymbol{u}=0\quad\text{in}\quad\Omega_f\times\mathcal{I}_T.$$

Integrating along the cross-section of Ω_f and considering (1c), we obtain on F

$$\nabla_{\boldsymbol{T}} \cdot \int_{-\frac{d}{2}}^{\frac{d}{2}} \boldsymbol{u}_{\boldsymbol{T}} dn = 0, \tag{4}$$

where

$$\boldsymbol{u}_{\boldsymbol{T}} = -\boldsymbol{K}_{\boldsymbol{T}} \lambda \nabla_{\boldsymbol{T}} p_n + \boldsymbol{K}_{\boldsymbol{T}} \lambda_w \nabla_{\boldsymbol{T}} p_c + \boldsymbol{K}_{\boldsymbol{T}} (\lambda_w \rho_w + \lambda_n \rho_n) \boldsymbol{g}_{\boldsymbol{T}}. \tag{5}$$

We set $\boldsymbol{u}_{_F} := \int_{-\frac{d}{2}}^{\frac{d}{2}} \boldsymbol{u}_{\boldsymbol{T}}$.

Similarly, in the reference system defined on the fracture Ω_f, Equation (3b) can be rewritten as

$$\Phi \frac{\partial S_w}{\partial t} + \nabla_{\boldsymbol{T}} \cdot \boldsymbol{u}_w + \nabla_{\boldsymbol{N}} \cdot \boldsymbol{u}_w = 0 \quad \text{in} \quad \Omega_f \times \mathcal{I}_T.$$

We assume that the porosity Φ is either invariant in the normal direction or averaged over the cross-section of Ω_f. Integrating along the cross-section of Ω_f and considering (1d), we obtain on F

$$\Phi \frac{\partial}{\partial t} \int_{-\frac{d}{2}}^{\frac{d}{2}} S_w dn + \nabla_{\boldsymbol{T}} \cdot \int_{-\frac{d}{2}}^{\frac{d}{2}} \boldsymbol{u}_{w_{\boldsymbol{T}}} dn = 0, \tag{6}$$

where

$$\boldsymbol{u}_{w_{\boldsymbol{T}}} = \boldsymbol{K}_{\boldsymbol{T}} \lambda_w \nabla_{\boldsymbol{T}} p_c - \boldsymbol{K}_{\boldsymbol{T}} \lambda_w \nabla_{\boldsymbol{T}} p_n + \boldsymbol{K}_{\boldsymbol{T}} \lambda_w \rho_w \boldsymbol{g}_{\boldsymbol{T}}. \tag{7}$$

We set $\boldsymbol{u}_{_{F_w}} := \int_{-\frac{d}{2}}^{\frac{d}{2}} \boldsymbol{u}_{w_T}$.

We introduce the pressure p_{n_F} and the saturation S_{w_F}, that represent the pressure of the non-wetting phase p_n and the saturation of the wetting phase S_w averaged over the cross-section of Ω_f, i.e.,

$$p_{n_F} := \frac{1}{d} \int_{-\frac{d}{2}}^{\frac{d}{2}} p_n dn, \quad S_{w_F} := \frac{1}{d} \int_{-\frac{d}{2}}^{\frac{d}{2}} S_w dn.$$

For what concerns the functions characterizing the fractured medium we adopt the notation $\lambda_{_F} := \lambda(S_{w_F})$, $\lambda_{w_F} := \lambda_w(S_{w_F})$ and $p_{c_F} := p_c(S_{w_F})$ and we set $\boldsymbol{K}_{_F} := d\, \boldsymbol{K}_{\boldsymbol{T}}$, $\Phi_{_F} := d\, \Phi$.

Integrating Equations (5) and (7) over the cross-section of the fracture Ω_f and substituting back into Equations (4) and (6) we obtain the reduced model equations. Consequently, the problem of the two-phase flow of immiscible fluids can be formulated as

$$-\nabla_{\boldsymbol{T}} \cdot \left\{ \boldsymbol{K}_{_F} \lambda_{_F} \nabla_{\boldsymbol{T}} p_{n_F} - \boldsymbol{K}_{_F} \lambda_{w_F} \frac{dp_{c_F}}{dS_{w_F}} \nabla_{\boldsymbol{T}} S_{w_F} - \boldsymbol{K}_{_F} (\lambda_{w_F} \rho_w + \lambda_{n_F} \rho_n) \boldsymbol{g}_{\boldsymbol{T}} \right\} = 0 \quad \text{in } F \times \mathcal{I}_T, \tag{8a}$$

$$\Phi_{_F} \frac{\partial S_{w_F}}{\partial t} + \nabla_{\boldsymbol{T}} \cdot \left\{ \boldsymbol{K}_{_F} \lambda_{w_F} \frac{dp_{c_F}}{dS_{w_F}} \nabla_{\boldsymbol{T}} S_{w_F} - \boldsymbol{K}_{_F} \lambda_{w_F} \nabla p_{n_F} + \boldsymbol{K}_{_F} \lambda_{w_F} \rho_w \boldsymbol{g}_{\boldsymbol{T}} \right\} = 0 \quad \text{in } F \times \mathcal{I}_T, \tag{8b}$$

$$p_{n_F} = \bar{g}_{_{D_p}} \quad \text{on} \quad \Gamma_{F_{D_p}} \times \mathcal{I}_T, \tag{8c}$$

$$\boldsymbol{u}_{_F} = \bar{Q}_{_{N_p}} \quad \text{on} \quad \Gamma_{F_{N_p}} \times \mathcal{I}_T, \tag{8d}$$

$$S_{w_F} = \bar{g}_{_{D_{S_w}}} \quad \text{on} \quad \Gamma_{F_{D_S}} \times \mathcal{I}_T, \tag{8e}$$

$$\boldsymbol{u}_{w_T} = \bar{Q}_{_{N_S}} \quad \text{on} \quad \Gamma_{F_{N_S}} \times \mathcal{I}_T \tag{8f}$$

$$S_{w_F} = \bar{S}_{w0} \quad \text{in} \quad F,\ t = 0, \tag{8g}$$

where $\bar{g}_{_{D_p}} := \frac{1}{d} \int_{-\frac{d}{2}}^{\frac{d}{2}} g_{_{D_p}}$, $\bar{g}_{_{D_{S_w}}} := \frac{1}{d} \int_{-\frac{d}{2}}^{\frac{d}{2}} g_{_{D_{S_w}}}$, $\bar{S}_{w0} := \frac{1}{d} \int_{-\frac{d}{2}}^{\frac{d}{2}} S_{w0}$ and $\bar{Q}_{_{N_p}} := \int_{-\frac{d}{2}}^{\frac{d}{2}} Q_{_{N_p}}$, $\bar{Q}_{_{N_S}} := \int_{-\frac{d}{2}}^{\frac{d}{2}} Q_{_{N_S}}$.

In the following section, we extend this model to a system consisting of a network of bi-dimensional fractures.

2.2 Discrete Fracture Network

Let us consider a space-time domain $\Omega \times \mathcal{I}_T$, where now Ω denotes the DFN and $\mathcal{I}_T := [0, T]$, with $T \in \mathbb{R}^+$, is the time interval. The DFN is the union of fractures, i.e., $\Omega := \bigcup_i F_i$, where $F_i \subset \mathbb{R}^3,\ i \in \mathcal{F} = \{1, \dots, N_F\}$ are planar polygons that can have arbitrary orientation in space. When fractures intersect, they form segments called traces $T_m,\ m \in \mathcal{T} = \{1, \dots, N_T\}$. In particular, we assume that each trace is given by the intersection of exactly two fractures, i.e. $T_m = \bar{F}_i \cap \bar{F}_j$; therefore, an injective map $\sigma : \mathcal{T} \to \mathcal{F} \times \mathcal{F}$ is defined between a trace index and a pair of fracture indices, thus $\sigma(m) = \{i, j\}$. Furthermore, we denote by $\mathcal{T}_i \subset \mathcal{T}$ the subset of trace indices corresponding to traces lying on the fracture F_i. We assume that there is no one-dimensional flow along the traces.

We denote by $\tilde{F}_i$ the fracture F_i without the traces T_m with $m \in \mathcal{T}_i$; therefore, the traces coincide with portions of the boundary of $\tilde{F}_i$ and we denote by $T_m^{\pm},\ m \in \mathcal{T}_i$ the two sides of these portions. Being $\boldsymbol{n}^i_{T_m}$ the outward pointing unit normal vector to each trace T_m on the fracture F_i, in what follows we define the jump of a vector quantity $\boldsymbol{w}_i$ across a trace $T_m \in \mathcal{T}_i$ on the fracture F_i as

$$[\![\boldsymbol{w}_i]\!]_{T_m} := \boldsymbol{w}_{i|_{T_m^+}} \cdot \boldsymbol{n}^i_{T_m} - \boldsymbol{w}_{i|_{T_m^-}} \cdot \boldsymbol{n}^i_{T_m}.$$

and we denote by $\nabla_{\boldsymbol{T}_i}$ the tangential component of the gradient on the plane defined by the fracture F_i.

We adopt the following assumption on the fractures that define the DFN:

A1. *In this model we assume that every fracture $F_i,\ i \in \mathcal{F}$ has the same width d and it consists of the same isotropic rock type, i.e. the porosity Φ_{F_i}, the absolute permeability $\boldsymbol{K}_{F_i} := K_{F_i}\boldsymbol{I} = dK\boldsymbol{I},\ K_{F_i}, K \in \mathbb{R}$ (where $\boldsymbol{I}$ denote the identity tensor), the capillary pressure curve $p_{c_{F_i}}$ and the relative permeability curves $k_{rn_{F_i}}$ and $k_{rw_{F_i}}$ are the same for all the fractures $F_i,\ i \in \mathcal{F}$.*

By virtue of Assumption 1, we do not need to use the subscript i when denoting the rock properties. Therefore, in what follows, we will simply write Φ_F, K_F, λ_F, λ_{w_F}, λ_{n_F}, p_{c_F} instead of Φ_{F_i}, K_{F_i}, λ_{F_i}, $\lambda_{w_{F_i}}$, $\lambda_{n_{F_i}}$, $p_{c_{F_i}}$.

Now we specify the coupling conditions at the fracture-fracture intersections. For the pressure equation, we require the balance of the jump of the normal component of the total velocities $\boldsymbol{u}_{F_i}$, $\boldsymbol{u}_{F_j}$ with respect to the fracture intersection $T_m,\ m \in \mathcal{T},\ \{i, j\} = \sigma(m)$; moreover, we impose the continuity of both the phase pressures $p_{\alpha_{F_i}}$, $p_{\alpha_{F_j}}$ at each trace $T_m,\ m \in \mathcal{T},\ \{i, j\} = \sigma(m)$. For the saturation equation, we require the balance of the jump of the normal component of the wetting phase velocities $\boldsymbol{u}_{w_{F_i}}$, $\boldsymbol{u}_{w_{F_j}}$ at each trace $T_m,\ m \in \mathcal{T}\ \{i, j\} = \sigma(m)$; moreover, we impose the continuity of the saturation of the wetting phase $S_{w_{F_i}}$, $S_{w_{F_j}}$ at each fracture intersection $T_m,\ m \in \mathcal{T}$. We underline that the continuity of the saturation can be imposed only under Assumption 1. Indeed, the continuity of the phase pressures on the trace T_m implies the continuity of the capillary pressure. Therefore, the saturations $S_{w_{i|_{T_m}}}$ and $S_{w_{j|_{T_m}}}$ must be such that the capillary pressures $p_{c_{i|_{T_m}}}$ and $p_{c_{j|_{T_m}}}$ are the same. If the two fractures F_i and F_j consist of different rock types, then the capillary pressure curves $p_{c_i}(S_{w_{F_i}})$ and $p_{c_j}(S_{w_{F_j}})$ are in general different. Consequently, the same capillary pressure value corresponds to different saturation values $S_{w_{i|_{T_m}}}$ and $S_{w_{j|_{T_m}}}$ [32]. Whereas, if the two fractures F_i and F_j consist of the same rock type, the capillary pressure curves coincide and consequently, we can simply require $S_{w_{i|_{T_m}}} = S_{n_{j|_{T_m}}}$.

The boundary of Ω is given by the union of the boundary of each fracture F_i, i.e. $\partial\Omega := \bigcup_{i=1}^{N_F} \partial F_i$. For simplicity, we consider only homogeneous Dirichlet boundary conditions for both the pressure of the non-wetting phase and the saturation of the wetting phase; therefore, $\Gamma_D := \partial\Omega$.

Under Assumption 1, the problem of the two-phase flow of immiscible fluids in $\Omega \times \mathcal{I}_T$ for the pressure of the non-wetting phase $p_{n_{F_i}}$ and the saturation of the wetting phase $S_{w_{F_i}}$ in each fracture $F_i,\ i = 1, \dots, N_F$ can be formulated as

$$-\nabla_{\boldsymbol{T}_i} \cdot \left\{ K_F \lambda_F \nabla_{\boldsymbol{T}_i} p_{n_{F_i}} - K_F \lambda_{w_F} \frac{dp_{c_F}}{dS_{w_{F_i}}} \nabla_{\boldsymbol{T}_i} S_{w_{F_i}} - K_F(\lambda_{w_F}\rho_w + \lambda_{n_F}\rho_n)\boldsymbol{g}_{\boldsymbol{T}_i} \right\} = 0 \quad \text{in } \tilde{F}_i \times \mathcal{I}_T, \tag{9a}$$

$$\Phi_{F}\frac{\partial S_{w_{F_i}}}{\partial t}+\nabla_{\boldsymbol{T}_i}\cdot\left\{K_{F}\lambda_{w_F}\frac{dp_{c_F}}{dS_{w_{F_i}}}\nabla_{\boldsymbol{T}_i}S_{w_{F_i}}-K_{F}\lambda_{w_F}\nabla p_{n_{F_i}}+K_{F}\lambda_{w_F}\rho_w\boldsymbol{g}_{\boldsymbol{T}_i}\right\}=0\quad\text{in }\tilde{F}_i\times\mathcal{I}_T, \tag{9b}$$

$$p_{n_{F_i}|_{T_m}}=p_{n_{F_j}|_{T_m}}\quad m\in\mathcal{T},\quad\{i,j\}=\sigma(m)\quad\forall t\in\mathcal{I}_T \tag{9c}$$

$$S_{w_{F_i}|_{T_m}}=S_{n_{F_j}|_{T_m}}\quad m\in\mathcal{T},\quad\{i,j\}=\sigma(m)\quad\forall t\in\mathcal{I}_T \tag{9d}$$

$$[\![\boldsymbol{u}_{F_i}]\!]_{T_m}=-[\![\boldsymbol{u}_{F_j}]\!]_{T_m}\quad m\in\mathcal{T},\quad\{i,j\}=\sigma(m)\quad\forall t\in\mathcal{I}_T, \tag{9e}$$

$$[\![\boldsymbol{u}_{w_{F_i}}]\!]_{T_m}=-[\![\boldsymbol{u}_{w_{F_j}}]\!]_{T_m}\quad m\in\mathcal{T},\quad\{i,j\}=\sigma(m)\quad\forall t\in\mathcal{I}_T, \tag{9f}$$

$$p_{n_{F_i}}=0\quad\text{on}\quad\partial F_i\in\Gamma_D\ \forall t\in\mathcal{I}_T, \tag{9g}$$

$$S_{w_{F_i}}=0\quad\text{on}\quad\partial F_i\in\Gamma_D\ \forall t\in\mathcal{I}_T, \tag{9h}$$

$$S_{w_{F_i}}=\tilde{S}_{w_{F_i}0}\quad\text{in}\quad F_i,\ t=0, \tag{9i}$$

where

$$\begin{aligned}\boldsymbol{u}_{F_i}&=-K_{F}\lambda_{F}\nabla_{\boldsymbol{T}_i}p_{n_{F_i}}+K_{F}\lambda_{w_F}\nabla_{\boldsymbol{T}_i}p_{c_{F_i}}+K_{F}(\lambda_{w_F}\rho_w+\lambda_{n_F}\rho_n)\boldsymbol{g}_{\boldsymbol{T}_i},\\ \boldsymbol{u}_{F_{w_i}}&=K_{F}\lambda_{w_F}\nabla_{\boldsymbol{T}_i}p_{c_{F_i}}-K_{F}\lambda_{w_F}\nabla_{\boldsymbol{T}_i}p_{n_{F_i}}+K_{F}\lambda_{w_F}\rho_w\boldsymbol{g}_{\boldsymbol{T}_i}.\end{aligned}$$

In what follows, we discretize the problem in time and in space following an approach similar to the one proposed by the authors in [31].

We will write the discrete formulation on a two-dimensional reference system of coordinates $\hat{\mathbf{x}}=(\hat{x},\hat{y})$ tangential to the fracture F_i. We denote by $\hat{\nabla}_i$ and by $\hat{\mathbf{g}}_i$, respectively, the operator corresponding to the tangential gradient $\nabla_{\boldsymbol{T}_i}$ and the vector corresponding to the tangential component of the gravity vector $\boldsymbol{g}_{\boldsymbol{T}_i}$ related to the fracture F_i in the new two-dimensional reference system.

3 Time discretization

Given the time interval $\mathcal{I}_T$, we subdivide it as $0=t^0<t^1<\cdots<t^C=T$ with $\Delta t^n:=t^n-t^{n-1}$, $n=1,\dots,C$. Then, we consider a sub-interval $[t^n,t^{n+1}]$. Moreover, we consider the function space $H^1_{0,\Gamma_D}(F_i)$ that represents the subspace of $H^1(F_i)$ of functions that have zero trace on $\partial F_i\cap\Gamma_D$. We assume that $p_{n_{F_i}}(t^n),S_{w_{F_i}}(t^n)\in H^1_{0,\Gamma_D}(F_i)$ are given $\forall i\in\mathcal{F}$ and that they satisfy the following continuity requirements

$$\begin{aligned}&p_{n_{F_i}}(t^n)_{|_{T_m}}=p_{n_{F_j}}(t^n)_{|_{T_m}}\quad m\in\mathcal{T},\quad\{i,j\}=\sigma(m)\quad\forall t\in\mathcal{I}_T,\\ &S_{w_{F_i}}(t^n)_{|_{T_m}}=S_{w_{F_j}}(t^n)_{|_{T_m}}\quad m\in\mathcal{T},\quad\{i,j\}=\sigma(m)\quad\forall t\in\mathcal{I}_T,\\ &[\![\boldsymbol{u}_{F_i}(t^n)]\!]_{T_m}=-[\![\boldsymbol{u}_{F_j}(t^n)]\!]_{T_m}\quad m\in\mathcal{T},\quad\{i,j\}=\sigma(m)\quad\forall t\in\mathcal{I}_T,\\ &[\![\boldsymbol{u}_{w_{F_i}}(t^n)]\!]_{T_m}=-[\![\boldsymbol{u}_{w_{F_j}}(t^n)]\!]_{T_m}\quad m\in\mathcal{T},\quad\{i,j\}=\sigma(m)\quad\forall t\in\mathcal{I}_T.\end{aligned} \tag{10}$$

In what follows, we denote by γ_{T_m} the trace operator related to the segment $T_m\subset F_i$ and the symbol $\langle\cdot,\cdot\rangle$ denotes the duality pairing between $H^{-\frac{1}{2}}(F_i)$ and $H^{\frac{1}{2}}(F_i)$. The weak formulation on a two-dimensional reference system tangential to the fracture F_i reads: given $p_{n_{F_i}}(t^n)$, $S_{w_{F_i}}(t^n)\in H^1_{0,\Gamma_D}(F_i)\ \forall i\in\mathcal{F}$ that satisfy (10), find $p_{n_{F_i}}(t^{n+1}),S_{w_{F_i}}(t^{n+1})\in H^1_{0,\Gamma_D}(F_i)$ such that for all $v_{p_{F_i}},v_{S_{F_i}}\in H^1_{0,\Gamma_D}(F_i)$, for $m\in\mathcal{T}_i$

$$a^{F_i}(S_{w_{F_i}}(t^{n+1});p_{n_{F_i}}(t^{n+1}),v_{p_{F_i}})=F^{P,F_i}(S_{w_{F_i}}(t^{n+1}),v_{p_{F_i}})+\langle[\![\boldsymbol{u}_{F_i}(t^{n+1})]\!]_{T_m},\gamma_{T_m}v_{p_{F_i}}\rangle, \tag{11a}$$

$$\begin{aligned}&\frac{c^{F_i}(S_{w_{F_i}}(t^{n+1}),v_{S_{F_i}})-c^{F_i}(S_{w_{F_i}}(t^n),v_{S_{F_i}})}{\Delta t}=\\ &\frac{1}{2}F^{S,F_i}(S_{w_{F_i}}(t^{n+1}),S_{w_{F_i}}(t^{n+1}),p_{n_{F_i}}(t^{n+1}),v_{S_{F_i}})-\frac{1}{2}\langle[\![\boldsymbol{u}_{w_{F_i}}(t^{n+1})]\!]_{T_m},\gamma_{T_m}v_{S_{F_i}}\rangle\\ &+\frac{1}{2}F^{S,F_i}(S_{w_{F_i}}(t^n),S_{w_{F_i}}(t^n),p_{n_{F_i}}(t^n),v_{S_{F_i}})-\frac{1}{2}\langle[\![\boldsymbol{u}_{w_{F_i}}(t^n)]\!]_{T_m},\gamma_{T_m}v_{S_{F_i}}\rangle,\end{aligned} \tag{11b}$$

with the coupling conditions

$$\begin{aligned}
&p_{n_{F_i}}(t^{n+1})_{|_{T_m}} = p_{n_{F_j}}(t^{n+1})_{|_{T_m}} \quad m \in \mathcal{T}, \quad \{i,j\} = \sigma(m) \quad \forall t \in \mathcal{I}_T,\\
&S_{w_{F_i}}(t^{n+1})_{|_{T_m}} = S_{w_{F_j}}(t^{n+1})_{|_{T_m}} \quad m \in \mathcal{T}, \quad \{i,j\} = \sigma(m) \quad \forall t \in \mathcal{I}_T,\\
&[\![\boldsymbol{u}_{F_i}(t^{n+1})]\!]_{T_m} = -[\![\boldsymbol{u}_{F_j}(t^{n+1})]\!]_{T_m} \quad m \in \mathcal{T}, \quad \{i,j\} = \sigma(m) \quad \forall t \in \mathcal{I}_T,\\
&[\![\boldsymbol{u}_{w_{F_i}}(t^{n+1})]\!]_{T_m} = -[\![\boldsymbol{u}_{w_{F_j}}(t^{n+1})]\!]_{T_m} \quad m \in \mathcal{T}, \quad \{i,j\} = \sigma(m) \quad \forall t \in \mathcal{I}_T.
\end{aligned} \tag{12}$$

We have defined $F^{P,F_i}(\cdot,\cdot)$ and $F^{S,F_i}(\cdot,\cdot,\cdot,\cdot)$ as

$$F^{P,F_i}(z,w) := -b^{F_i}(z,w) - g^{F_i}(z,w),$$

$$F^{S,F_i}(z_1,z_2,v,w) := -d^{F_i}(z_1;z_2,w) - e^{F_i}(z_1,v,w) - f^{F_i}(z_1,w).$$

The quantities appearing in Equation (11) are defined as follows.

Let $a^{F_i}(\cdot;\cdot,\cdot)$ be the global form bilinear and symmetric in its second and third arguments defined as

$$a^{F_i}(z;v,w) := \int_{F_i} \hat{\nabla}_i v^T K_{_F} \lambda_{_F}(z) \hat{\nabla}_i w \ \mathrm{d}\hat{\mathbf{x}}.$$

Moreover, $b^{F_i}(\cdot,\cdot)$ and $g^{F_i}(\cdot,\cdot)$ are defined as

$$\begin{aligned}
b^{F_i}(z,w) &:= -\int_{F_i} \hat{\nabla}_i z^T K_{_F} \lambda_{w_F}(z) \frac{dp_{c_F}(z)}{dS_{w_{F_i}}} \hat{\nabla}_i w \ \mathrm{d}\hat{\mathbf{x}},\\
g^{F_i}(z,w) &:= -\int_{F_i} \hat{\boldsymbol{g}}_i^T K_{_F} (\lambda_{w_F}(z)\rho_w + \lambda_{n_F}(z)\rho_n) \hat{\nabla}_i w \ \mathrm{d}\hat{\mathbf{x}}.
\end{aligned}$$

$c^{F_i}(\cdot,\cdot)$ is a global symmetric and bilinear form and $d(\cdot;\cdot,\cdot)$ is a global form symmetric and bilinear in its second and third arguments defined as

$$\begin{aligned}
c^{F_i}(v,w) &:= \int_{F_i} \Phi_{_F} \ v \ w \ \mathrm{d}\hat{\mathbf{x}},\\
d^{F_i}(z_1;z_2,w) &:= -\int_{F_i} \hat{\nabla}_i z_2^T K_{_F} \lambda_{w_F}(z_1) \frac{dp_{c_F}(z_1)}{dS_{w_{F_i}}} \hat{\nabla}_i w \ \mathrm{d}\hat{\mathbf{x}}.
\end{aligned}$$

Moreover, $e^{F_i}(\cdot;\cdot,\cdot)$ and $f^{F_i}(\cdot,\cdot)$ are defined as

$$\begin{aligned}
e^{F_i}(z_1;v,w) &:= \int_{F_i} \hat{\nabla}_i v^T K_{_F} \lambda_{w_F}(z_1) \hat{\nabla}_i w \ \mathrm{d}\hat{\mathbf{x}},\\
f^{F_i}(z_1,w) &:= -\int_{F_i} \hat{\boldsymbol{g}}_i^T K_{_F} \lambda_{w_F}(z_1) \rho_w \hat{\nabla}_i w \ \mathrm{d}\hat{\mathbf{x}}.
\end{aligned}$$

We introduce the function space

$$V = \big\{ v \in H^1_{0,\Gamma_D}(F_i) \ \forall i \in \mathcal{F} : \ \gamma_{_{T_m}} v_{_{F_i}} = \gamma_{_{T_m}} v_{_{F_j}} \ \forall m \in \mathcal{T}, \ \{i,j\} = \sigma(m) \big\}.$$

Functions in V automatically satisfy the coupling conditions. We remark that in what follows to lighten the notation, we adopt the symbols $p_n,\ S_w \in V$ to indicate the global pressure of the non-wetting phase and the global saturation of the wetting phase in the whole DFN. Therefore, the weak formulation reads: given $p_n(t^n), S_w(t^n) \in V$, find $p_n(t^{n+1}), S_w(t^{n+1}) \in V$ such that for all $v_p, v_S \in V$, for $m \in \mathcal{T}_i$ and $i \in \mathcal{F}$.

$$\sum_{i=1}^{N_F} a^{F_i}(S_{w_{F_i}}(t^{n+1}); p_{n_{F_i}}(t^{n+1}), v_{p_{F_i}}) = \sum_{i=1}^{N_F} F^{P,F_i}(S_{w_{F_i}}(t^{n+1}), v_{p_{F_i}}), \tag{13a}$$

$$\sum_{i=1}^{N_F} \frac{c^{F_i}(S_{w_{F_i}}(t^{n+1}), v_{S_{F_i}}) - c^{F_i}(S_{w_{F_i}}(t^{n}), v_{S_{F_i}})}{\Delta t} = \tag{13b}$$

$$\frac{1}{2}\sum_{i=1}^{N_F} F^{S,F_i}(S_{w_{F_i}}(t^{n+1}), S_{w_{F_i}}(t^{n+1}), p_{n_{F_i}}(t^{n+1}), v_{S_{F_i}})$$
$$+\frac{1}{2}\sum_{i=1}^{N_F} F^{S,F_i}(S_{w_{F_i}}(t^{n}), S_{w_{F_i}}(t^{n}), p_{n_{F_i}}(t^{n}), v_{S_{F_i}}).$$

System of equations (13) is fully implicit and coupled; moreover, it cannot be solved directly because of its non-linearity. Firstly, we linearize Equation (13b) with respect to the saturation using Newton-Raphson method and then we adopt an iterative IMPIS formulation for solving equation (13a) and the linearized version of equation (13b).

Given the initial iterates $p_n(t^{n+1},0) := p_n(t^n)$ and $S_w(t^{n+1},0) := S_w(t^n)$, we construct a sequence $S_w(t^{n+1},r+1) := S_w(t^{n+1},r) + \delta S_w(t^{n+1},r+1),\ r \geq 0$, by solving at each iteration sequentially the linearized problems (1) and (2) that follow.

1. Given $S_w(t^{n+1},r), p_n(t^{n+1},r) \in V$, find $\delta S_w(t^{n+1},r+1) \in V$, $r \geq 0$ such that the following holds true $\forall v_S \in V$

$$\begin{aligned}
&\sum_{i=1}^{N_F} c^{F_i}(\delta S_{w_{F_i}}(t^{n+1},r+1), v_{S_{F_i}}) \\
&+\frac{\Delta t}{2}\sum_{i=1}^{N_F} \tilde{F}^{S,F_i}(S_{w_{F_i}}(t^{n+1},r), \delta S_{w_{F_i}}(t^{n+1},r+1), p_{n_{F_i}}(t^{n+1},r), v_{S_{F_i}}) = \\
&-\sum_{i=1}^{N_F} c^{F_i}(S_{w_{F_i}}(t^{n+1},r), v_{S_{F_i}}) \\
&+\frac{\Delta t}{2}\sum_{i=1}^{N_F} F^{S,F_i}(S_{w_{F_i}}(t^{n+1},r), S_{w_{F_i}}(t^{n+1},r), p_{n_{F_i}}(t^{n+1},r), v_{S_{F_i}}) \\
&+\sum_{i=1}^{N_F} c^{F_i}(S_{w_{F_i}}(t^{n}), v_{S_{F_i}}) + \frac{\Delta t}{2}\sum_{i=1}^{N_F} F^{S,F_i}(S_{w_{F_i}}(t^{n}), S_{w_{F_i}}(t^{n}), p_{n_{F_i}}(t^{n}), v_{S_{F_i}}),
\end{aligned} \tag{14}$$

where

$$\tilde{F}^{S,F_i}(z_1,z_2,v,w) := d^{F_i}(z_1;z_2,w) + l^{F_i}(z_1;z_2,w) + m^{F_i}(z_1;v;z_2,w) + n^{F_i}(z_1;z_2,w),$$

$$\begin{aligned}
l^{F_i}(z_1;z_2,w) &:= -\int_{F_i} z_2\ (\hat{\nabla}_i z_1)^T K_F b_F(z_1)\hat{\nabla}_i w\ \mathrm{d}\hat{\mathbf{x}}, \\
m^{F_i}(z_1;v;z_2,w) &:= \int_{F_i} z_2\ (\hat{\nabla}_i v)^T K_F r_F(z_1)\ \hat{\nabla}_i w\ \mathrm{d}\hat{\mathbf{x}}, \\
n^{F_i}(z_1;z_2,w) &:= -\int_{F_i} z_2\ \hat{\boldsymbol{g}}_i^T K_F r_F(z_1)\rho_w\ \hat{\nabla}_i w\ \mathrm{d}\hat{\mathbf{x}},
\end{aligned}$$

$$b_F := \frac{d}{dS_{w_{F_i}}}\Big(\lambda_{w_F}\frac{dp_{c_F}}{dS_{w_{F_i}}}\Big), \quad r_F := \frac{d\lambda_{w_F}}{dS_{w_{F_i}}}.$$

2. *Given* $S_w(t^{n+1},r+1) = S_w(t^{n+1},r) + \delta S_w(t^{n+1},r+1)$, *find* $p_n(t^{n+1},r+1) \in V$, $r \geq 0$, *such that the following holds true* $\forall v_p \in V$

$$\sum_{i=1}^{N_F} a^{F_i}(S_{w_{F_i}}(t^{n+1},r+1); p_{n_{F_i}}(t^{n+1},r+1), v_{p_{F_i}}) = \sum_{i=1}^{N_F} F^{P,F_i}(S_{w_{F_i}}(t^{n+1},r+1), v_{p_{F_i}}). \tag{15}$$

4 Space discretization

Let $\mathcal{T}_\delta$ be a globally conforming tessellation of Ω that satisfies all the regularity requirements needed by the virtual element method [35] and such that the diameter δ_E of each element $E \in \mathcal{T}_E$ is bounded by a finite constant $\delta > 0$. We denote by $\hat{\mathbb{P}}_k(E)$ the space of polynomials of degree $k \in \mathbb{N}$ with respect to the reference system tangential to the fracture F to which the element E belongs.

We introduce the elementwise $H^1(E)$-orthogonal projection operator $\hat{\Pi}^\nabla_{k,E} : H^1(E) \to \hat{\mathbb{P}}_k(E)$, defined in the bi-dimensional reference system tangential to E as follows

$$\int_E \nabla \hat{\Pi}^\nabla_{k,E} v \cdot \hat{\nabla} p \, \mathrm{d}\hat{\mathbf{x}} = \int_E \hat{\nabla} v \cdot \hat{\nabla} p \, \mathrm{d}\hat{\mathbf{x}} \quad \forall p \in \hat{\mathbb{P}}_k(E), \; v \in H^1(E),$$

and

$$\int_{\partial E} \hat{\Pi}^\nabla_{k,E} v \, \mathrm{d}s = \int_{\partial E} v \, \mathrm{d}s \quad \text{if } k = 1,$$
$$\int_E \hat{\Pi}^\nabla_{k,E} v \, \mathrm{d}\hat{\mathbf{x}} = \int_E v \, \mathrm{d}\hat{\mathbf{x}} \quad \text{if } k > 1,$$

where the differential operator $\hat{\nabla}$ is defined with respect to a two-dimensional reference system tangential to the fracture F to which the element E belongs. Moreover, we denote by $\hat{\Pi}^0_{k,E}$ the elementwise $L^2(E)$-orthogonal projection operator on $\hat{\mathbb{P}}_k(E)$ and by $\hat{\Pi}^0{}_{k-1,E}\hat{\nabla}$ the elemetwise $L^2(E)$-orthogonal projection operator of the gradient on $\hat{\mathbb{P}}_{k-1}(E) \times \hat{\mathbb{P}}_{k-1}(E)$. Let $\hat{\Pi}^\nabla_k$, $\hat{\Pi}^0_k$ and $\hat{\Pi}^0_{k-1}\hat{\nabla}$ be the corresponding global projection operators.

Given $k \geq 1$ the order of the virtual element method, we consider the spaces:

$$\hat{\mathbb{B}}_k(\partial E) := \Big\{ v \in C^0(\partial E) : v_{|e} \in \hat{\mathbb{P}}_k(e) \; \forall e \in \mathcal{E}_{\delta,E} \Big\},$$
$$\hat{\mathcal{M}}^*_k(E) := \Big\{ \hat{m} : \hat{m}(\hat{x}, \hat{y}) = \frac{(\hat{x} - \hat{x}_E)^{\alpha_{\hat{x}}} (\hat{y} - \hat{y}_E)^{\alpha_{\hat{y}}}}{\delta_E^{\alpha_{\hat{x}} + \alpha_{\hat{y}}}}, \alpha_{\hat{x}} + \alpha_{\hat{y}} = k \Big\},$$

where $\hat{\mathbb{P}}_k(e)$ denotes the space of polynomials of degree k on each edge e in the set of the boundary edges $\mathcal{E}_{\delta,E}$ of the element E in the tangential reference system and $(\hat{x}_E, \hat{y}_E)$ are the coordinates of the centroid of E.

Then, the local two-dimensional virtual element space $\hat{\mathcal{V}}^{k,E}_\delta$ on the plane tangential to the element E of dimension $N^{k,E}_{dof}$ is defined as

$$\begin{aligned} \hat{\mathcal{V}}^{k,E}_\delta := \Big\{ & v \in H^1(E) : v_{|\partial E} \in \hat{\mathbb{B}}_k(\partial E), \; \hat{\Delta} v_{|E} \in \hat{\mathbb{P}}_k(E), \\ & \int_E v \; p \, \mathrm{d}\hat{\mathbf{x}} = \int_E \hat{\Pi}^\nabla_{k,E} v \; p \, \mathrm{d}\hat{\mathbf{x}} \;\; \forall p \in \hat{\mathcal{M}}^*_{k-1}(E) \cup \hat{\mathcal{M}}^*{}_k(E) \Big\}. \end{aligned} \tag{16}$$

Again, the differential operators are defined with respect to the bi-dimensional reference system tangential to E.

On each element E, we select the set of scaled monomials $\hat{\mathcal{M}}_k(E)$ as a basis for the local polynomial space $\hat{\mathbb{P}}_k(E)$

$$\hat{\mathcal{M}}_k(E) := \Big\{ \hat{m} : \hat{m}(\hat{x}, \hat{y}) = \frac{(\hat{x} - \hat{x}_E)^{\alpha_{\hat{x}}} (\hat{y} - \hat{y}_E)^{\alpha_{\hat{y}}}}{\delta_E^{\alpha_{\hat{x}} + \alpha_{\hat{y}}}}, 0 \leq \alpha_{\hat{x}} + \alpha_{\hat{y}} \leq k \Big\}.$$

Given, $v \in \hat{\mathcal{V}}^{k,E}_\delta$, we choose the following standard set of degrees of freedom

- values of v at the vertices of the polygon E;
- for $k > 1$, the values of v at the $k-1$ internal points of the $k+1$ points of the Gauss-Lobatto quadrature rule on each edge $e \in \mathcal{E}_{\delta,E}$;

- for $k > 1$, the momentum up to order $k-2$ of v in E, i.e., $\frac{1}{|E|}\int_E v\ \hat{m}\ d\hat{\boldsymbol{x}}, \quad \hat{m} \in \hat{\mathcal{M}}_{k-2}(E)$.

We point out that $N_{dof}^{k,E}$ equals the total number of the selected degrees of freedom; moreover, thanks to the particular choice of the local virtual element space (16) and of the set of degrees of freedom defined above, the projection operators $\hat{\Pi}_{k,E}^{\nabla} v, \hat{\Pi}_{k,E}^{0} v$ and $\hat{\Pi}_{k-1,E}^{0}\hat{\nabla} v$ are all computable.

As a basis for the local virtual element space, we choose the Lagrangian basis function with respect to the degrees of freedom.

We denote by $\mathcal{T}_{\delta,i}$ the restriction of the tessellation $\mathcal{T}_\delta$ to the fracture F_i. Then, the virtual element space on $\mathcal{T}_{\delta,i}$ is obtained from the local spaces $\hat{\mathcal{V}}_\delta^{k,E}$ as follows

$$\hat{V}_{\delta,i}^k := \Big\{ v \in H_0^1(F_i) : v_{|E} \in \hat{\mathcal{V}}_\delta^{k,E}\ \forall E \in \mathcal{T}_{\delta,i} \Big\}.$$

Since the tessellation $\mathcal{T}_\delta$ is globally conforming, we can define the global discrete space V_δ^k as

$$V_\delta^k = \{ v \in V : v_{|F_i} \in \hat{V}_{\delta,i}^k \}.$$

For generality, we select two distinct virtual element spaces for the pressure of the non-wetting phase and for saturation of the wetting phase, denoting as k_p and as k_S the selected values of the integer k for the pressure and the saturation, respectively. As a consequence, the related global virtual element spaces are denoted by $V_\delta^{k_p}$ and $V_\delta^{k_S}$, respectively. In the numerical examples, we will only consider the case $k_p = k_S = k$.

Given a generic $v_\delta \in V_\delta^k$, we denote its restriction on the fracture F_i with $v_{\delta_{F_i}}$. Following the approach presented by the authors in [31], the fully discrete virtual element variational formulation of (14) and (15) reads:

1. *Given* $S_{w_\delta}(t^n),\ S_{w_\delta}(t^{n+1}, r) \in V_\delta^{k_S}$ *and* $p_{n_\delta}(t^n),\ p_{n_\delta}(t^{n+1}, r) \in V_\delta^{k_p}$, *find* $S_{w_\delta}(t^{n+1}, r+1) \in V_\delta^{k_S}$, $r \geq 0$, *such that the following relation holds true* $\forall v_{S_\delta} \in V_\delta^{k_S}$

$$\begin{aligned}
&\sum_{i=1}^{N_F} c_\delta^{F_i}(\delta S_{w_{\delta F_i}}(t^{n+1}, r+1), v_{S_{\delta F_i}}) \\
&+ \frac{\Delta t}{2}\sum_{i=1}^{N_F} \tilde{F}_\delta^{S,F_i}(S_{w_{\delta F_i}}(t^{n+1}, r), \delta S_{w_{\delta F_i}}(t^{n+1}, r+1), p_{n_{\delta F_i}}(t^{n+1}, r), v_{S_{\delta F_i}}) \\
&= -\sum_{i=1}^{N_F} c_\delta^{F_i}(S_{w_{\delta F_i}}(t^{n+1}, r), v_{S_{\delta F_i}}) \\
&+ \frac{\Delta t}{2}\sum_{i=1}^{N_F} F_\delta^{S,F_i}(S_{w_{\delta F_i}}(t^{n+1}, r), S_{w_{\delta F_i}}(t^{n+1}, r), p_{n_{\delta F_i}}(t^{n+1}, r), v_{S_{\delta F_i}}) \\
&+ \sum_{i=1}^{N_F} c_\delta^{F_i}(S_{w_{\delta F_i}}(t^n), v_{S_{\delta F_i}}) + \frac{\Delta t}{2}\sum_{i=1}^{N_F} F_\delta^{S,F_i}(S_{w_{\delta F_i}}(t^n), S_{w_{\delta F_i}}(t^n), p_{n_{\delta F_i}}(t^n), v_{S_{\delta F_i}}),
\end{aligned} \tag{17}$$

where $S_{w_\delta}(t^{n+1}, 0) := S_{w_\delta}(t^n)$, $p_{n_\delta}(t^{n+1}, 0) := p_{n_\delta}(t^n)$ *and*

$$\begin{aligned}
F_\delta^{S,F_i}(z_1, z_2, v, w) &:= -d_\delta^{F_i}(z_1; z_2, w) - e_\delta^{F_i}(z_1, v, w) - f_\delta^{F_i}(z_1, w), \\
\tilde{F}_\delta^{S,F_i}(z_1, z_2, v, w) &:= d_\delta^{F_i}(z_1; z_2, w) + l_\delta^{F_i}(z_1; z_2, w) + m_\delta^{F_i}(z_1; v; z_2, w) + n_\delta^{F_i}(z_1; z_2, w).
\end{aligned}$$

2. *Given* $S_{w_\delta}(t^{n+1}, r+1) \in V_\delta^{k_S}$, *find* $p_{n_\delta}(t^{n+1}, r+1) \in V_\delta^{k_p}$, $r \geq 0$, *such that the following holds true* $\forall v_{p_\delta} \in V_\delta^{k_p}$

$$\sum_{i=1}^{N_F} a_\delta^{F_i}(S_{w_{\delta F_i}}(t^{n+1}, r+1); p_{n_{\delta F_i}}(t^{n+1}, r+1), v_{p_{\delta F_i}}) = \sum_{i=1}^{N_F} F_\delta^{P,F_i}(S_{w_{\delta F_i}}(t^{n+1}, r+1), v_{p_{\delta F_i}}), \tag{18}$$

with

$$F_\delta^{P,F_i}(z, w) := -b_\delta^{F_i}(z, w) - g_\delta^{F_i}(z, w).$$

The global quantities appearing in (17) and (18) are locally defined according to the choices discussed in [31] and they can be constructed elementwise using the projection operators previously defined. In particular, the local form $a_\delta^{E,F_i}(\cdot;\cdot,\cdot)$, $b_\delta^{E,F_i}(\cdot;\cdot,\cdot)$ and $c_\delta^{E,F_i}(\cdot,\cdot)$ must satisfy polynomial consistency and stability defined as in [31].

First of all we focus on the variational formulation (18) related to the pressure of the non-wetting phase.

The local form a_δ^{E,F_i} is defined as

$$a_\delta^{E,F_i}(z;v,w) := \int_E [\hat{\Pi}^0_{k_p-1,E}\hat{\nabla}_i v]^T \; K_{_F}\lambda_{_F}(\hat{\Pi}^0_{k_S,E}z) \; [\hat{\Pi}^0_{k_p-1,E}\hat{\nabla}_i w] \; \mathrm{d}\hat{\mathbf{x}} + S^{E,F_i}\Big(z;(I-\hat{\Pi}^\nabla_{k_p,E})v,(I-\hat{\Pi}^\nabla_{k_p,E})w\Big),$$

with the admissible stabilizing form S^{E,F_i}

$$S^{E,F_i}\Big(z;(I-\hat{\Pi}^\nabla_{k_p,E})v,(I-\hat{\Pi}^\nabla_{k_p,E})w\Big) := ||K_{_F}\lambda_{_F}(\hat{\Pi}^0_{k_S,E}z)||_{L^\infty(E)} \sum_{l=1}^{N_{dof}^{k_p,E}} \mathrm{dof}_l^{k_p}\Big((I-\hat{\Pi}^\nabla_{k_p,E})v\Big)\mathrm{dof}_l^{k_p}\Big((I-\hat{\Pi}^\nabla_{k_p,E})w\Big),$$

where I denotes the identity operator and $\mathrm{dof}_l^{k_p}(\cdot)$ is the operator selecting the l-th degree of freedom of $v \in \mathcal{V}_\delta^{k_p,E}$.

The terms $b_\delta^{E,F_i}(\cdot,\cdot)$ and $g_\delta^{E,F_i}(\cdot,\cdot)$ are defined as follows

$$b_\delta^{E,F_i}(z,w) := -\int_E [\hat{\Pi}^0_{k_S-1,E}\hat{\nabla}_i z]^T \; K_{_F}\lambda_{w_F}(\hat{\Pi}^0_{k_S,E}z)\frac{dp_{c_F}(\hat{\Pi}^0_{k_S,E}z)}{dS_{w_{F_i}}} \; [\hat{\Pi}^0_{k_p-1,E}\hat{\nabla}_i w] \; \mathrm{d}\hat{\mathbf{x}},$$

$$g_\delta^{E,F_i}(z,w) := -\int_E \hat{\boldsymbol{g}}_i^T \; K_{_F}\Big(\lambda_{w_F}(\hat{\Pi}^0_{k_S,E}z)\rho_w + \lambda_{n_F}(\hat{\Pi}^0_{k_S,E}z)\rho_n\Big)[\hat{\Pi}^0_{k_p-1,E}w] \; \mathrm{d}\hat{\mathbf{x}}.$$

Now, we focus on the variational formulation (17) related to the saturation of the wetting phase.

The local form c_δ^{E,F_i} is defined as

$$c_\delta^{E,F_i}(v,w) := \int_E \Phi_{_F}\hat{\Pi}^0_{k_S,E}v \; \hat{\Pi}^0_{k_S,E}w \; \mathrm{d}\hat{\mathbf{x}} + M^{E,F_i}\Big((I-\hat{\Pi}^0_{k_S,E})v,(I-\hat{\Pi}^0_{k_S,E})w\Big),$$

with the stabilizing bilinear form M^{E,F_i}

$$M^{E,F_i}\Big((I-\hat{\Pi}^0_{k_S,E})v,(I-\hat{\Pi}^0_{k_S,E})w\Big) := ||\Phi_{_F}||_{L^\infty(E)}\delta_E^2 \sum_{l=1}^{N_{dof}^{k_S,E}} \mathrm{dof}_l^{k_S}\Big((I-\hat{\Pi}^0_{k_S,E})v\Big)\mathrm{dof}_l^{k_S}\Big((I-\hat{\Pi}^0_{k_S,E})w\Big),$$

where $\mathrm{dof}_l^{k_S}(\cdot)$ is the operator selecting the l-th degree of freedom of $v \in \mathcal{V}_\delta^{k_S,E}$.

Moreover, the local form d_δ^{E,F_i} is defined as

$$d_\delta^{E,F_i}(z_1;z_2,w) := -\int_E [\hat{\Pi}^0_{k_S-1,E}\hat{\nabla}_i z_2]^T \; K_{_F}\lambda_{w_F}(\hat{\Pi}^0_{k_S,E}z_1)\frac{dp_{c_F}(\hat{\Pi}^0_{k_S,E}z_1)}{dS_{w_{F_i}}} \; [\hat{\Pi}^0_{k_S-1,E}\hat{\nabla}_i w] \; \mathrm{d}\hat{\mathbf{x}} + D^{E,F_i}\Big(z_1;(I-\hat{\Pi}^\nabla_{k_S,E})z_2,(I-\hat{\Pi}^\nabla_{k_S,E})w\Big),$$

with the stabilizing bilinear form D^{E,F_i}

$$D^{E,F_i}\Big(z_1;(I-\hat{\Pi}^\nabla_{k_S,E})z_2,(I-\hat{\Pi}^\nabla_{k_S,E})w\Big) :=$$

$$\Big|\Big|K_{_F}\lambda_{w_F}(\hat{\Pi}^0_{k_S,E}z_1)\frac{dp_{c_F}(\hat{\Pi}^0_{k_S,E}z_1)}{dS_{w_{F_i}}}\Big|\Big|_{L^\infty(E)}\sum_{l=1}^{N^{k_S,E}_{dof}}\mathrm{dof}_l^{k_S}\Big((I-\hat{\Pi}^\nabla_{k_S,E})z_2\Big)\mathrm{dof}_l^{k_S}\Big((I-\hat{\Pi}^\nabla_{k_S,E})w\Big).$$

The terms $e_\delta^{E,F_i}(\cdot;\cdot,\cdot)$, $f_\delta^{E,F_i}(\cdot,\cdot)$, $l_\delta^{E,F_i}(\cdot;\cdot,\cdot)$, $m_\delta^{E,F_i}(\cdot;\cdot;\cdot,\cdot)$ and $n_\delta^{E,F_i}(\cdot;\cdot,\cdot)$ are defined as follows

$$\begin{aligned}
e_\delta^{E,F_i}(z_1;v,w) &:= \int_E [\hat{\Pi}^0_{k_S-1,E}\hat{\nabla}_i v]^T\ K_{_F}\lambda_{w_F}(\hat{\Pi}^0_{k_S,E}z_1)\ [\hat{\Pi}^0_{k_S-1,E}\ \hat{\nabla}_i w]\ \mathrm{d}\hat{\mathbf{x}},\\
f_\delta^{E,F_i}(z_1,w) &:= -\int_E \hat{\boldsymbol{g}}_i^T\ K_{_F}\lambda_{w_F}(\hat{\Pi}^0_{k_S,E}z_1)\rho_w\ [\hat{\Pi}^0_{k_S-1,E}\hat{\nabla}_i w]\ \mathrm{d}\hat{\mathbf{x}},\\
l_\delta^{E,F_i}(z_1;z_2,w) &:= -\int_E z_2\ [\hat{\Pi}^0_{k_S-1,E}\hat{\nabla}_i z_1]^T K_{_F} b_{_F}(\hat{\Pi}^0_{k_S,E}z_1)[\hat{\Pi}^0_{k_S-1,E}\hat{\nabla}_i w]\ \mathrm{d}\hat{\mathbf{x}},\\
m_\delta^{E,F_i}(z_1;v;z_2,w) &:= \int_E z_2\ [\hat{\Pi}^0_{k_p-1,E}\hat{\nabla}_i v]^T K_{_F} r_{_F}(\hat{\Pi}^0_{k_S,E}z_1)\ [\hat{\Pi}^0_{k_S-1,E}\hat{\nabla}_i w]\ \mathrm{d}\hat{\mathbf{x}},\\
n_\delta^{E,F_i}(z_1;z_2,w) &:= -\int_E z_2\ \hat{\boldsymbol{g}}_i^T K_{_F} r_{_F}(\hat{\Pi}^0_{k_S,E}z_1)\rho_w\ [\hat{\Pi}^0_{k_S-1,E}\hat{\nabla}_i w]\ \mathrm{d}\hat{\mathbf{x}}.
\end{aligned}$$

Remark 1. One of the key features of the virtual element approach is the possibility to easily enforce continuity conditions at the fracture-fracture interface. Indeed, since the tessellation $\mathcal{T}_\delta$ is globally conforming, the continuity conditions are automatically satisfied by the selected functional spaces. In particular, the use of unique degrees of freedom across the various domains avoid the use of Lagrangian multipliers to impose the matching conditions.

5 Numerical results

In this section, firstly, we describe the procedure adopted to construct a globally conforming mesh and then we present numerical results in order to validate the method. In particular, we consider several discrete fracture networks of increasing complexity and characterized by different features.

5.1 Mesh construction

In order to construct a globally conforming mesh $\mathcal{T}_\delta$, we perform the following three steps.

1. (Local mesh) We generate a polygonal tessellation $\mathcal{T}_i^{loc}$ on each fracture F_i independently. This mesh is not necessarily conformed with respect to the traces of the considered fracture. Indeed, we do not take into account the trace positions or any conformity requirement.

2. (Local conformity) On each fracture, we create a new node both when a trace intersect an element edge and at the trace tips. If the trace tip lies inside an element, we extend the trace segment until it intersects the edge of the mesh element. We remark that in the extension process, no changes are made to the geometry of the fracture intersections. Finally, we split the elements that intersect the traces generating new elements. In this way, we obtain a locally conforming mesh $\mathcal{T}_i^{cnf}$ with respect to the fracture traces in which all traces are covered by element edges.

3. (Global conformity) On each trace T_m, $\{i,j\}=\sigma(m)$, we take from $\mathcal{T}_i^{cnf}$ and $\mathcal{T}_j^{cnf}$ the union set of mesh nodes lying on the trace segment. From this set we take the local missing nodes in each $\mathcal{T}_i^{cnf}$ and $\mathcal{T}_j^{cnf}$, and we add them on the trace mesh edges of $\mathcal{T}_i^{cnf}$ and $\mathcal{T}_j^{cnf}$, respectively. In this way, we generate a globally conforming tessellation. We recall that the VEM allows elements having aligned edges and an arbitrary number of edges.

A more detailed explanation of this approach can be found in [19].

5.2 Test 1: 2-fracture DFN with known analytical solution

In Test 1, we analyse the convergence of the proposed method on a two-fracture DFN in a problem with a known solution. In particular, we focus on the non degenerate case in which the saturation equation is a parabolic convection-diffusion equation with respect to the saturation of the wetting phase. As done in [31], given the parabolic nature of the coupled non-linear problem (9), we evaluate the spatial discretization errors for both the pressure and the saturation at the end of the time interval by means of the L^2-norm and the H^1-seminorm. As explained in [31], given that the time integration error is sufficiently small, on the basis of the convergence estimates in [35] and [36] on a simpler problem and on the basis of the best interpolation estimates for VEM spaces of order k, the best order of convergences that can be expected with respect to the number of elements $\mathcal{N}_\delta$ of the tessellation are $O(\mathcal{N}_\delta)^{-\frac{k+1}{2}}$ and $O(\mathcal{N}_\delta)^{-\frac{k}{2}}$ in L^2-norm and in H^1-seminorm, respectively. We underline that, since the VEM solutions for the pressure of the non-wetting phase p_{n_δ} and for the saturation of the wetting phase S_{w_δ} cannot be evaluated in arbitrary points inside each element, in the computation of the errors we consider their polynomial projections $\hat{\Pi}^0_{k_p} p_{n_\delta}$ and $\hat{\Pi}^0_{k_p} S_{w_\delta}$.

In this test, we consider a time interval $\mathcal{I}_T = [0, 1]$ $[s]$ and a simple DFN Ω consisting of two fractures F_1 and F_2 and one trace T defined as

$$
\begin{aligned}
F_1 &= \{(x, y, z) \in \mathbb{R}^3 : -1 \leq x \leq 1, -1 \leq y \leq 1, z = 0\},\\
F_2 &= \{(x, y, z) \in \mathbb{R}^3 : -1 \leq x \leq 1, -1 \leq z \leq 1, y = 0\},\\
T &= \{(x, y, z) \in \mathbb{R}^3 : y = 0, z = 0, -1 \leq x \leq 1\}.
\end{aligned}
$$

The exact solutions are given by the following analytical expressions

$$
\begin{aligned}
p_{n_{ex},1}(x, y, z, t) &= 10^5 \cdot \Big(\frac{t}{100}(|y| + x^4) + \frac{1}{2}\Big)\ [Pa],\\
S_{w_{ex},1}(x, y, z, t) &= \frac{1}{2} + \frac{1}{6}tx^4\ [-],\\
p_{n_{ex},2}(x, y, z, t) &= 10^5 \cdot \Big(-\frac{g}{100}z + \frac{t}{100}(-|z| + x^4) + \frac{1}{2}\Big)\ [Pa],\\
S_{w_{ex},2}(x, y, z, t) &= \frac{1}{2} + \frac{1}{6}tx^4\ [-].
\end{aligned}
$$

In particular, we notice that the saturations $S_{w_{ex},1}$ and $S_{w_{ex},2}$ attain values within the interval $[0, 1]$ in the given space-time domain and the pressures $p_{n_{ex},1}$ and $p_{n_{ex},2}$ have a realistic magnitude of $10^5[Pa]$. It can also be easily seen that at the interface T the pressures and the saturations satisfy the coupling conditions (9c) and (9d), respectively. Moreover, the coupling conditions on the total velocity (9e) and on the velocity of the wetting phase (9f) are satisfied as well.

The physical data of the problem are reported in Table 1; the data are taken from [25] and they are selected to be close to realistic values.

Porosity	$\Phi = 0.3$ $[-]$
Absolute permeability	$K = 10^{-10}$ $[m^2]$
Residual saturations	$S_{wr} = 0,\ S_{nr} = 0$ $[-]$
Viscosities	$\mu_w = 0.001,\ \mu_n = 0.001$ $[Pa \cdot s]$
Densities	$\rho_w = \rho_n = 1000$ $[Kg/m^3]$
Brooks-Corey parameters	$\mu = 1.0$ $[-],\ p_d = 5000$ $[Pa]$

Table 1: Test 1: porous medium and fluids data.

We impose Dirichlet boundary conditions; since it is not easy to construct an analytical solution having zero source/sink term, in this Test 1 we consider the presence of the terms

$q(x, y, z, t)$ and $q_w(x, y, z, t)$ in (9). Therefore, given the exact solutions of the pressures and of the saturations and the parameters of the porous medium and of the two fluids, we compute the source/sink terms $q(x, y, z, t)$ and $q_w(x, y, z, t)$.

For convergence study, we consider four different meshes; they are generated according to the procedure explained in Section 5.1 starting from locally conforming tessellation on each fracture consisting of triangles ($\mathcal{T}_{\delta_T}$), squares ($\mathcal{T}_{\delta_S}$), polygons ($\mathcal{T}_{\delta_P}$) and Voronoi cells with no Lloyd iterations ($\mathcal{T}_{\delta_V}$), respectively. In particular, the single-fracture triangle mesh is constructed using the Triangle library [37], whereas the single-fracture polygonal and Voronoi grids are generated using the mesh generator PolyMesher [38]. A representative of each family of meshes is shown in Figure 1.

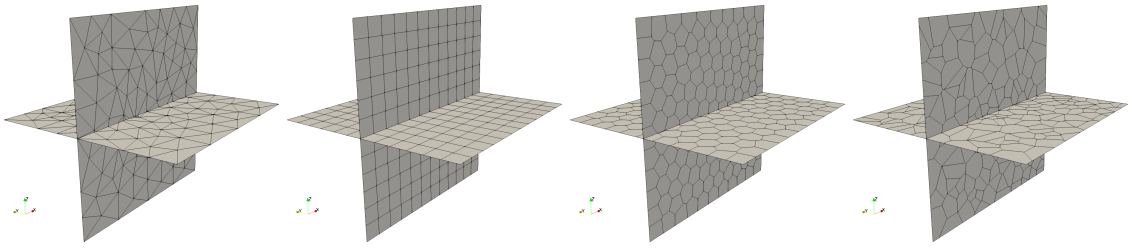

(a) Triangle ($\mathcal{T}_{\delta_T}$) (b) Square ($\mathcal{T}_{\delta_S}$) (c) Polygon ($\mathcal{T}_{\delta_P}$) (d) Voronoi ($\mathcal{T}_{\delta_V}$)

Figure 1: Test 1: meshes.

In particular, we evaluate the errors at the end of the prescribed time interval for four different refinements of each tessellation having $\mathcal{N}_{\delta_1}$, $\mathcal{N}_{\delta_2}$, $\mathcal{N}_{\delta_3}$ and $\mathcal{N}_{\delta_4}$ elements, respectively. More precisely, $\mathcal{N}_{\delta_1} = 80$, $\mathcal{N}_{\delta_2} = 338$, $\mathcal{N}_{\delta_3} = 1314$ and $\mathcal{N}_{\delta_4} = 5068$ for the tessellation $\mathcal{T}_{\delta_T}$, $\mathcal{N}_{\delta_1} = 72$, $\mathcal{N}_{\delta_2} = 288$, $\mathcal{N}_{\delta_3} = 1300$ and $\mathcal{N}_{\delta_4} = 5000$ for the tessellation $\mathcal{T}_{\delta_S}$, $\mathcal{N}_{\delta_1} = 86$, $\mathcal{N}_{\delta_2} = 314$, $\mathcal{N}_{\delta_3} = 1308$ and $\mathcal{N}_{\delta_4} = 5112$ for the tessellation $\mathcal{T}_{\delta_P}$, and $\mathcal{N}_{\delta_1} = 88$, $\mathcal{N}_{\delta_2} = 316$, $\mathcal{N}_{\delta_3} = 1326$ and $\mathcal{N}_{\delta_4} = 5116$ for the tessellation $\mathcal{T}_{\delta_V}$. For each one of the four refinements we consider the following time steps: $\Delta t_1 = 0.2$ $[s]$, $\Delta t_2 = 0.1$ $[s]$, $\Delta t_3 = 0.05$ $[s]$ and $\Delta t_4 = 0.025$ $[s]$. As already specified in [31], even if we have considered the Crank-Nicolson scheme that is unconditionally stable for the time discretization, we cannot choose an arbitrary time step. Indeed, we need to guarantee that the initial guess of the Newton-Raphson scheme is sufficiently close to the solution for the convergence of the method.

In Figures 2-3 we show the convergence curves of the relative error in the L^2-norm (below) and in the H^1-seminorm (above) a $t = 1$ $[s]$ in a log-log scale for the VEM of order $k = 1$ and $k = 3$ for both the pressure of the non-wetting phase and the saturation of the wetting phase, respectively. We observe that the slopes of the dotted lines follow the expected convergence rate for both the pressure and the saturation. Consequently, we conclude that the method behaves as expected. Furthermore, the method proves to be stable with respect to the different considered element shapes.

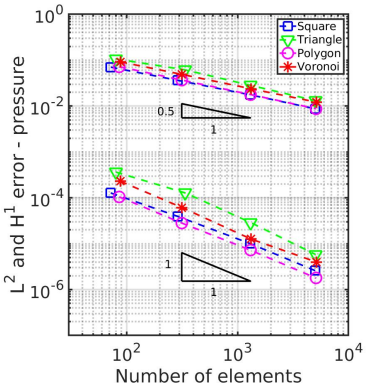

(a) Pressure p_n, $k = 1$ L^2-norm and H^1-seminorm relative error

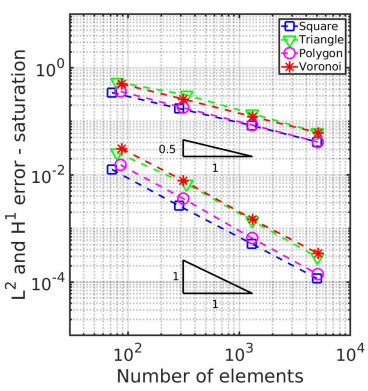

(b) Saturation S_w, $k = 1$ L^2-norm and H^1-seminorm relative error

Figure 2: Test 1: Pressure and Saturation, $k = 1$.

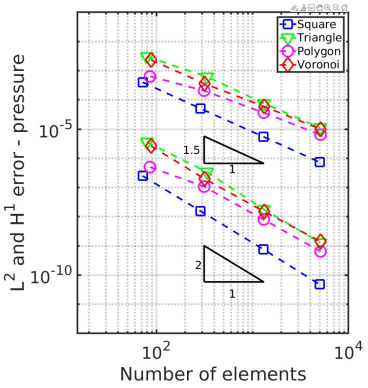

(a) Pressure p_n, $k = 3$ L^2-norm and H^1-seminorm relative error

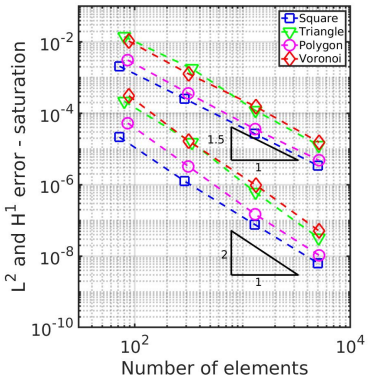

(b) Saturation S_w, $k = 3$ L^2-norm and H^1-seminorm relative error

Figure 3: Test 1: Pressure and Saturation, $k = 3$.

5.3 Test 2: Stair DFN for the McWhorter and Sunada bidirectional problem

In Test 2 we consider the bidirectional McWhorter and Sunada problem [39]. This is a well known problem for the two-phase flow of immiscible fluids in porous media in which a non-wetting phase fluid (oil) is horizontally displaced by a wetting phase fluid (water) pumped at one side of a one-dimensional horizontal domain representing a reservoir. In this problem the saturation equation has a parabolic nature, because the capillary pressure p_c is not neglected. Nevertheless, the diffusive term can vanish when the saturation approaches either the value zero or one. Consequently, the saturation equation can be "doubly" degenerate parabolic [40]. The McWhorter and Sunada problem can be subdivided into the bidirectional flow problem and the unidirectional flow problem. The former is a degenerate diffusive dominated problem, whereas the latter is a degenerate diffusive-convection dominated problem. In particular, we focus on the bidirectional case. In this originally mono-dimensional problem the flow occurs in a one-dimensional horizontal reservoir, $x \in (0, +\infty)$, initially filled by the non-wetting phase (oil), i.e. $S_w(x, 0) = S_w^0 = 0, \forall x > 0$. The saturation of the wetting phase (water) at the

left end of the domain ($x = 0$) is kept equal to S_{w0} (with $S_{w0} > S_w^0$), while the right end is impermeable. Neither sources nor gravity terms are considered. This gives rise to a bidirectional displacement in which the non-wetting phase (oil) is draining only at $x = 0$. As pointed out, this problem is originally mono-dimensional. However, it is possible to solve a 2D version of this problem in a domain $(x_i, x_f) \times (y_i, y_f)$ assuming a constant solution on the y direction. In [31], using the proposed VEM approach, the authors have solved this particular problem (hereafter referred to as MS problem) on a bi-dimensional rectangular domain $\Omega_{MS} = (0, 0.3) \times (0, 1)$ $[m^2]$ and in the time interval $\mathcal{I}_T = [0, 1000]$ $[s]$ imposing the boundary and the initial conditions reported in Table 2, where $\boldsymbol{n}_{\Omega_{MS}}$ denotes the unit normal pointing outward associated with the boundary of the domain Ω_{MS}. Then, the author have compared the numerical solution with the semi-analytical solution computed by means of the approach proposed in [41].

$y = 0$ and $y = 1$ $[m]$	$\boldsymbol{u} \cdot \boldsymbol{n}_{\Omega_{MS}} = 0$ $[m \cdot s^{-1}]$, $\boldsymbol{u}_w \cdot \boldsymbol{n}_{\Omega_{MS}} = 0$ $[m \cdot s^{-1}]$
$x = 0$ $[m]$	$p_n = 2 \cdot 10^5$ $[Pa]$, $S_w = 0.8$ $[-]$
$x = 0.3$ $[m]$	$\boldsymbol{u} \cdot \boldsymbol{n}_{\Omega_{MS}} = 0$ $[m \cdot s^{-1}]$, $S_w = 0$ $[-]$
$x \in \Omega_{MS}$, $t = 0$ $[s]$	$S_w(x, 0) = 0$ $[-]$

Table 2: Test 2: boundary and initial conditions for the bidirectional McWhorter and Sunada problem (MS).

In this work, we consider the same time interval $\mathcal{I}_T$ and we start from the bi-dimensional rectangular domain Ω_{MS} to construct a simplified version of a DFN. This will be the new considered space domain for the resolution of the bidirectional McWhorter-Sunada problem. More precisely, we proceed as follows. We subdivide the bi-dimensional rectangular domain Ω_{MS} into six rectangles having dimension 0.05 $[m] \times 1$ $[m]$. Then, we fold the domain in the 3D space to construct a three-step stair that geometrically can be interpreted as a 6-fracture DFN in which each fracture consists of a rectangle of dimension 0.05 $[m] \times 1$ $[m]$. The total rise of the stair along the z-axis is 0.15 $[m]$. In this way, the original bidirectional McWhorter and Sunada problem describing a two-phase flow of immiscible fluids in a rectangular porous media turns into a problem describing a two-phase flow of immiscible fluids in a poro-fractured media modeled through a discrete fracture network involving 6 fractures (hereafter referred to as MSDFN problem). We denote by Ω_{MSDFN} this DFN domain. In Figure 4, we show the original rectangular domain Ω_{MS} and the new DFN domain Ω_{MSDFN}. The fractures are numbered from 1 to 6 starting from the origin of the axis.

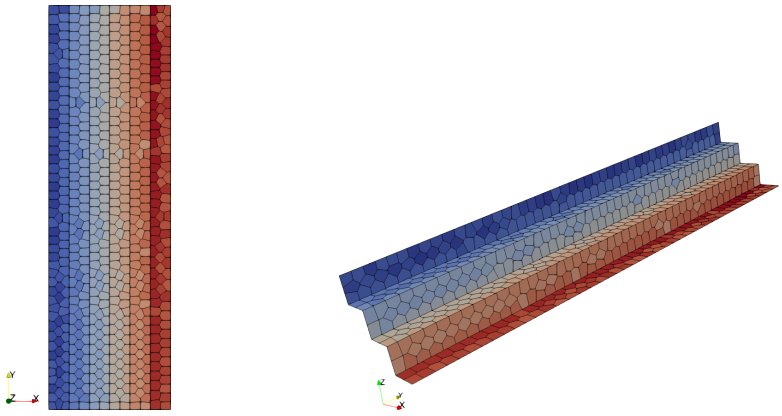

(a) MS (b) MSDFN

Figure 4: Test 2: example of domains and meshes for the MS problem and the MSDFN problem.

The purpose of this test is to compare the results obtained for the three-dimensional domain Ω_{MSDFN} with the ones obtained for the bi-dimensional domain Ω_{MS}. We proceed as follows: on

each of the six fractures in the 3D space and on each of the six rectangles in the bi-dimensional rectangular domain, we generate a locally conforming tessellation so that there is a one-to-one correspondence between the mesh in the i-th fracture of Ω_{MSDFN} and the mesh in the i-th rectangle of Ω_{MS}. Then, using the technique explained in Section 5.1, we generate a globally conforming tessellation both on the DFN and on the bi-dimensional rectangular domain. In this way, we obtain the same mesh for both the MS problem and MSDFN problem and this allows us to compare both the numerical solutions. In Figure 4 we report an example of globally conforming mesh of 618 elements constructed from six different locally conforming meshes consisting of polygonal elements for both the MS problem and the MSDFN problem.

We select the same boundary and initial conditions reported in Table 2 for the MS problem, but properly adapted to the new DFN configuration Ω_{MSDFN}. We denote by $\boldsymbol{n}_{\Omega_{MSDFN}}$ the unit normal pointing outward associated with the boundary of the domain Ω_{MSDFN}. The DFN domain Ω_{MSDFN} is initially completely filled by the non-wetting phase fluid, i.e. $S_w(x,y,z,t) = 0\ [-],\ (x,y,z) \in \Omega_{MSDFN},\ t = 0\ [s]$. Moreover, we set Dirichlet boundary conditions $p_n(x,y,z,t) = 2{\cdot}10^5\ [Pa]$ and $S_w(x,y,z,t) = 0.8\ [-]$, for $x = 0\ [m],\ 0 \le y \le 1\ [m]$ and $z = 0.15\ [m]$ (starting edge), $t \in \mathcal{I}_T$ and Dirichlet boundary condition $S_w(x,y,z,t) = 0\ [-]$ and Neumann boundary condition $\mathbf{u}(x,y,z,t){\cdot}\boldsymbol{n}_{\Omega_{MSDFN}} = 0\ [m{\cdot}s^{-1}]$, for $x = 0.15\ [m],\ 0 \le y \le 1\ [m]$ and $z = 0\ [m]$ (ending edge), $t \in \mathcal{I}_T$. On all the remaining edges, we set homogeneous Neumann boundary conditions $\mathbf{u} \cdot \boldsymbol{n}_{\Omega_{MSDFN}} = 0\ [m \cdot s^{-1}]$ and $\mathbf{u}_w \cdot \boldsymbol{n}_{\Omega_{MSDFN}} = 0\ [m \cdot s^{-1}]$. Furthermore, we set $q(x,y,z,t) = q_w(x,y,x,t) = 0\ [s^{-1}]$, for $(x,y,z) \in \Omega_{MSDFN}, t \in \mathcal{I}_T$ as in the model equations (9).

We notice that the initial saturation of the wetting phase equals zero. Consequently, in the temporal evolution of the numerical solution, it can happen that the numerical saturation of the wetting phase attains small negative values in certain points of the domain that are very close to points where it attains zero values. Since this is not acceptable neither from a mathematical point of view nor from a physical point of view, we have adopted a local correction. In particular, as better explained in [31], we force to zero only the values of the saturation that are negative on the quadrature nodes used to evaluate the different physical parameters in the computation. However, we do not change the global solution. As a result we accept small negative values of the numerical saturation near the front.

In what follows, we consider five different tests. In the first test (MSDFN1) we neglect the gravity term ($g = 0\ [m \cdot s^{-2}]$), whereas in the remaining ones, unlike the original McWhorter and Sunada problem, we activate the gravity term ($g \neq 0\ [m \cdot s^{-2}]$). Moreover, in the second test (MSDFN2) we set $\rho_{w,MSDFN2} = 1000\ [Kg/m^3]$ and $\rho_{n,MSDFN2} = 400\ [Kg/m^3]$, in the third test (MSDFN3) we set $\rho_{w,MSDFN3} = 400\ [Kg/m^3]$ and $\rho_{n,MSDFN3} = 1000\ [Kg/m^3]$, in the fourth test (MSDFN4) we set $\rho_{w,MSDFN4} = \rho_{n,MSDFN4} = 1000\ [Kg/m^3]$ and, finally, in the fifth test (MSDFN5) we set $\rho_{w,MSDFN5} = \rho_{n,MSDFN5} = 400\ [Kg/m^3]$.

The parameters that describe the properties of the porous medium and of the two fluids are reported in Table 3 for the MS problem and for all the other five test problems MSDFN1, MSDFN2, MSDFN3, MSDFN4 and MSDFN5.

Porosity	$\Phi = 0.3\ [-]$
Absolute permeability	$K = 10^{-10}\ [m^2]$
Residual saturations	$S_{wr} = 0,\ S_{nr} = 0\ [-]$
Viscosities	$\mu_w = 0.001,\ \mu_n = 0.020\ [Pa \cdot s]$
Brooks-Corey parameters	$\mu = 2.0\ [-],\ p_d = 1000\ [Pa]$

Table 3: Test 2: porous medium and fluids data for the MS problem and the MSDFN(1-5) problems.

In the MSDFN1 problem, since the gravity equals zero, we expect that both the numerical pressure of the non-wetting phase and the numerical saturation of the wetting phase coincide with the ones computed in the MS problem. This check allows us to verify if the proposed

method is working properly. In the MSDFN4 and MSDFN5 problems, we expect that the saturations of the wetting phase coincide with the one computed in the MS problem since $g \neq 0$, but $\rho_w = \rho_n$. Nevertheless, we expect the pressure of the non-wetting phase to be different. Instead, in the MSDFN3 and MSDFN4 problems, we expect different behaviour for both the saturation and the pressure with respect to the MS problem $g \neq 0$, but $\rho_w \neq \rho_n$. In particular, in case $\rho_w > \rho_n$, we expect the saturation front to move faster with respect to the reference MSDFN1 problem, whereas, in case $\rho_n > \rho_w$, we expect the opposite behaviour.

In Figures 5-6, we compare qualitatively the graph of the numerical solutions for the pressure of the non-wetting phase and the saturation of the wetting phase computed for the MS problem and the MSDFN(1-5) problems. In particular, we show the numerical solutions obtained at $T = 1000$ $[s]$ with a time step $\Delta t = 1.25[s]$ using a VEM spatial discretization of order $k = 1$ and a globally conforming mesh of 9600 elements (19184 nodes) constructed from six different locally conforming meshes consisting of polygonal elements as shown in Figure 4. In Figure 5 the colouring is proportional to the values of the pressure and in Figure 6 the colouring is proportional to the values of the saturation. We can see that, as explained above, the numerical saturations exhibit slightly negative values close to the points in the region of transition from high gradients to zero gradients. Comparing Figures 5a-5b and Figures 6a-6b we can see qualitatively that both the pressure and the saturation solutions are the same for the MS and the MSDFN1 problems. We underline that the results reported in Figures 5a-6a for the MS problem have been already verified by the authors in [31]. Moreover, comparing Figures 6e-6f and Figures 5e-5f we can see qualitatively that the saturation solutions are the same for the MSDFN4, MSDFN5 and MS problems, whereas the pressure solutions differ. Finally, comparing Figure 6b and Figure 6c, as expected we can see that the saturation front moves faster in MSDFN2 problem than in MSDFN1 problem due to the gravity assisting effect; whereas comparing Figure 6b and Figure 6d, we can see that the saturation front moves slower in MSDFN3 problem than in MSDFN1 problem due to the gravity opposing effect [42, 43].

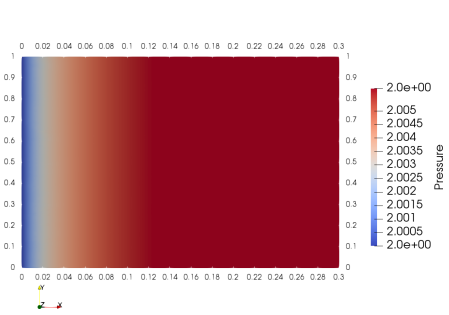

(a) MS problem

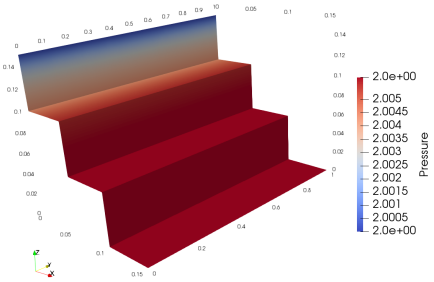

(b) MSDFN1 problem ($g = 0$)

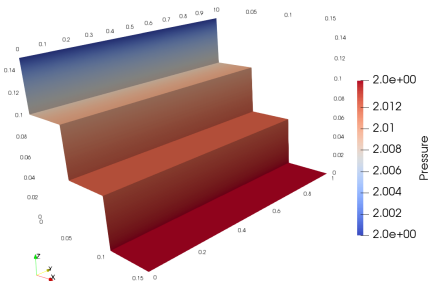

(c) MSDFN2 problem ($g \neq 0$)
$\rho_w > \rho_n$, with $\rho_w = 1000$ Kg/m^3 and
$\rho_n = 400$ Kg/m^3

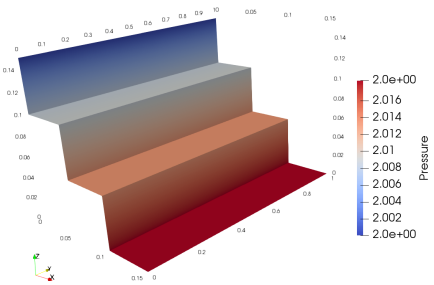

(d) MSDFN3 problem ($g \neq 0$)
$\rho_n > \rho_w$, with $\rho_n = 1000$ Kg/m^3 and
$\rho_w = 400$ Kg/m^3

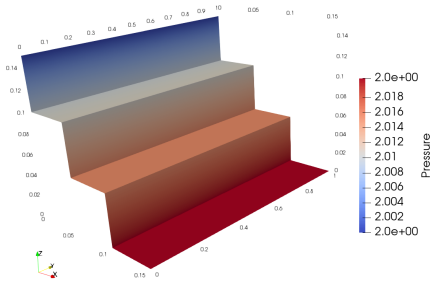

(e) MSDFN4 problem ($g \neq 0$)
$\rho_w = \rho_n = 1000$ Kg/m^3

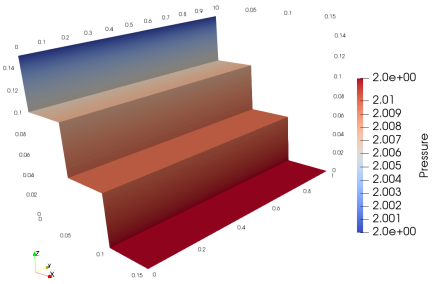

(f) MSDFN5 problem ($g \neq 0$)
$\rho_n = \rho_w = 400$ Kg/m^3

Figure 5: Test 2: pressure of the non-wetting phase p_n [bar] for MS problem and MSDFN(1-5) problems.

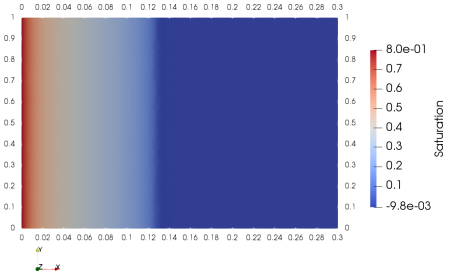

(a) MS problem

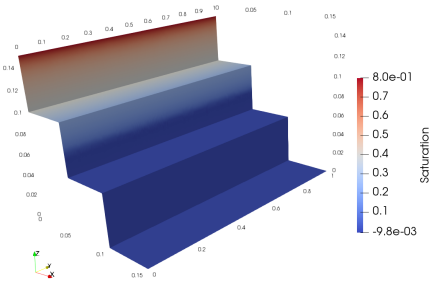

(b) MSDFN1 problem ($g = 0$)

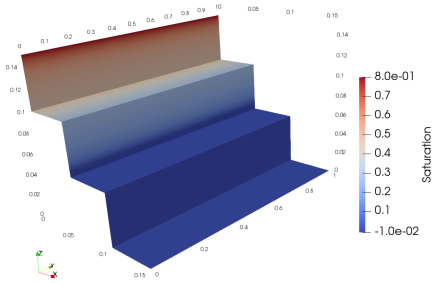

(c) MSDFN2 problem ($g \neq 0$)
$\rho_w > \rho_n$, with $\rho_w = 1000$ Kg/m^3 and
$\rho_n = 400$ Kg/m^3

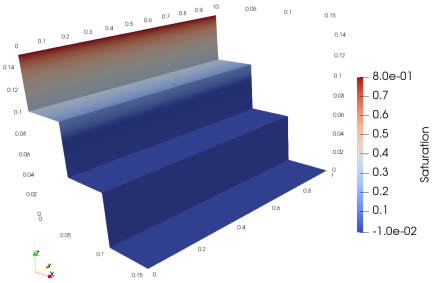

(d) MSDFN3 problem ($g \neq 0$)
$\rho_n > \rho_w$, with $\rho_n = 1000$ Kg/m^3 and
$\rho_w = 400$ Kg/m^3

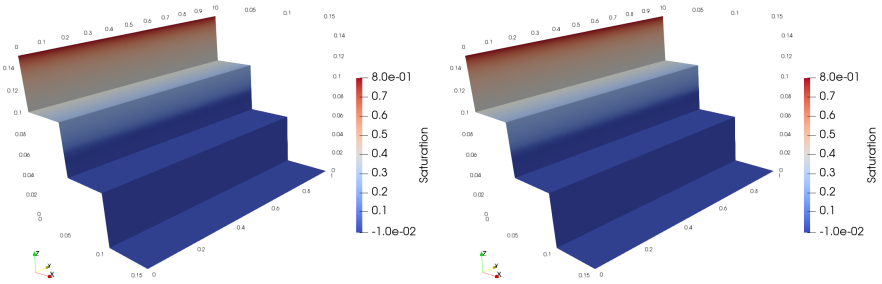

(e) MSDFN4 problem ($g \neq 0$)
$\rho_w = \rho_n = 1000$ Kg/m^3

(f) MSDFN5 problem ($g \neq 0$)
$\rho_n = \rho_w = 400$ Kg/m^3

Figure 6: Test 2: saturation of the wetting phase S_w $[-]$ for MS problem and MSDFN(1-5) problems.

In Figure 8, we plot the profile of the pressure of the non-wetting phase and of the saturation of the wetting phase along a line given by the intersection of the domain with a plane close to $y = 0.5$. This allows us to compare more quantitatively the pressure and the saturation profiles displayed qualitatively in the previous Figures 5-6. In Figures 7-8, we can see that in case the gravity is neglected the profiles of the pressure of the non-wetting phase and the profiles of the saturation of the wetting phase of the MS problem and the MSDFN1 problem coincide. The same holds true for the saturation profiles of the MSDFN4 and MSDFN5 problems; whereas, the same does not hold true for their pressure profiles as expected. Indeed, in both the two cases, the pressure of the non-wetting phase achieves higher values with respect to the ones achieved in the MSDFN1 problem. From Figures 7b, 7d and 7f, we can notice that in fractures 2, 4 and 6, since $\rho_w = \rho_n$ and the tangential component of the gravity acceleration vector gives no contribution, the pressure profile of the MSDFN4 and MSDFN5 problems are parallel to the pressure profile of the MSDFN1 problem. For what concerns, the MSDFN2 and the MSDFN3 problems, from Figures 8a, 8b and 8c, we can see that the saturation of the wetting phase profile achieves higher values and lower values, respectively, than in the MSDFN1 problem. Furthermore, from Figures 7d, 7e and 7f, we notice that in fractures 4 and 6, where the saturation equal zero and the tangential component of the gravity acceleration vector gives no contribution, all the pressure profiles are constant. Whereas, in fracture 5, where the saturation equal zero but the tangential component of the gravity acceleration vector gives contribution, the pressure profiles of the MSDFN3 and MSDFN4 are parallel since $\rho_{n,MSDFN3} = \rho_{n,MSDFN4}$. However, the one of the MSDFN4 achieves higher values since $\rho_{w,MSDFN4} > \rho_{w,MSDFN3}$. Similarly, the pressure profiles of the MSDFN2 and MSDFN5 are parallel since $\rho_{n,MSDFN2} = \rho_{n,MSDFN5}$, but the one of the MSDFN2 achieves higher values since $\rho_{w,MSDFN2} > \rho_{w,MSDFN5}$.

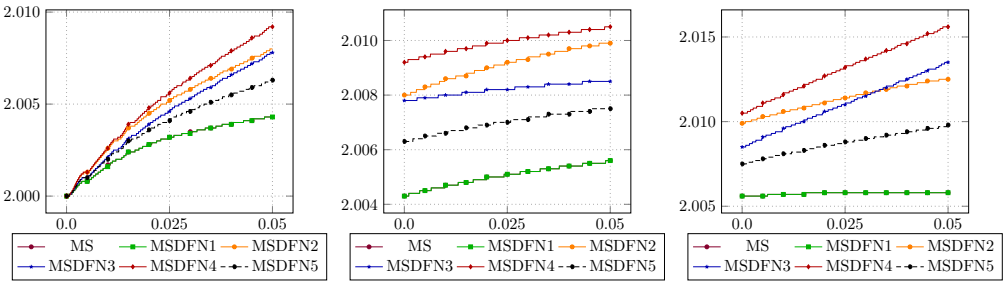

(a) p_n [bar], fracture 1

(b) p_n [bar], fracture 2

(c) p_n [bar], fracture 3

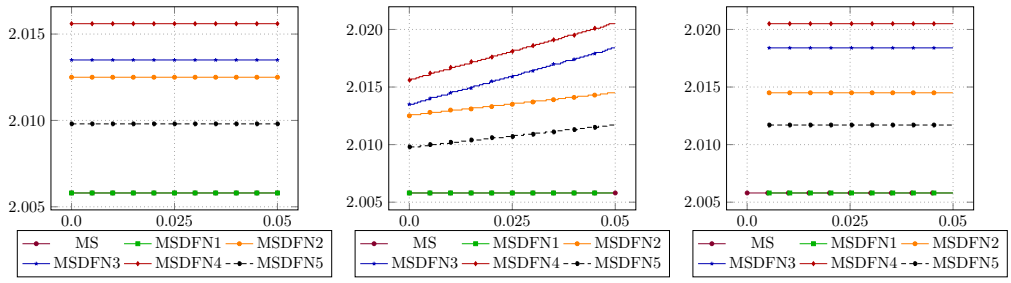

(d) p_n [bar], fracture 4 (e) p_n [bar], fracture 5 (f) p_n [bar], fracture 6

Figure 7: Test 2: profile of the pressure of the non-wetting phase p_n [bar] along a line given by the intersection of the first three fractures with a plane close to $y = 0.5$ for the MS problem and the MSDFN(1-5) problems.

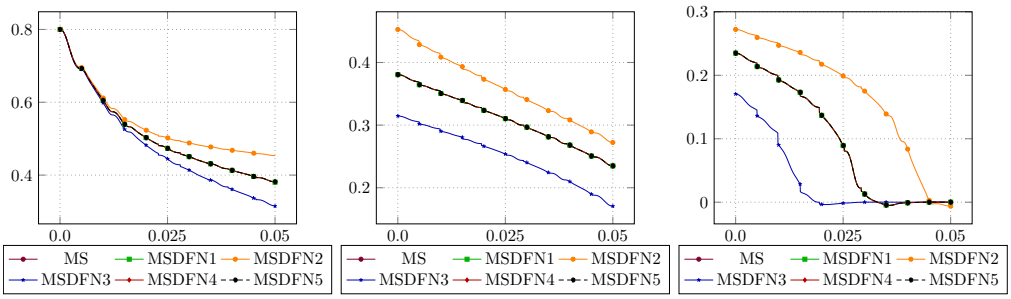

(a) S_w [-], fracture 1 (b) S_w [-], fracture 2 (c) S_w [-], fracture 3

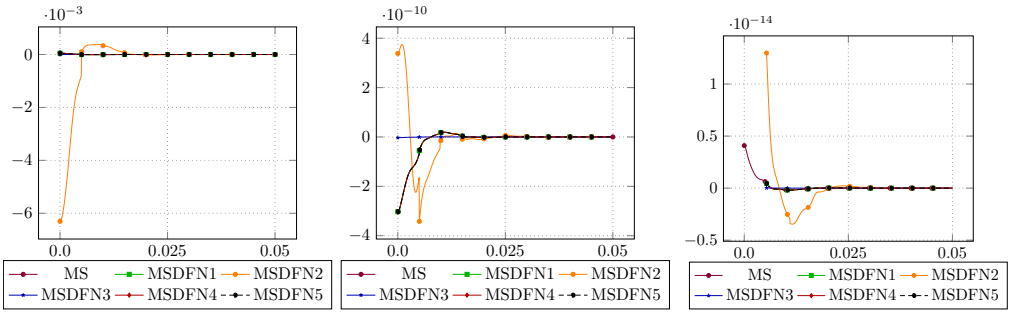

(d) S_w [-], fracture 4 (e) S_w [-], fracture 5 (f) S_w [-], fracture 6

Figure 8: Test 2: profile of the saturation of the wetting phase S_w [-] along a line given by the intersection of the first three fractures with a plane close to $y = 0.5$ for the MS problem and the MSDFN(1-5) problems.

5.4 Test 3: 6-fracture DFN

In Test 3, we generalize the McWhorter and Sunada bidirectional problem discussed in Test 2 to the simulation of counter-current imbibition problems in a DFN.

Imbibition is a mechanism used to enhance oil recovery in fractured reservoir [43]. It involves the inflow of the wetting phase in the porous medium and the consequent displacement of the non-wetting phase under the forces of the capillary pressure and the gravity. According to the flow direction the imbibition can be co-current or counter-current; in the former, the wetting phase pushes the non-wetting phase in the same direction, whereas in the latter, the wetting phase pushes the non-wetting phase in the opposite direction. The co-current imbibition is

typically faster and more efficient with respect to the counter-current imbibition, however the latter is often the only possible imbibition mechanism if the reservoir is exposed only from one side to the wetting phase filling it.

In this test, we focus on the simulation of the counter-current imbibition problem in fractured reservoir modeled as a 6-fracture DFN. The domain description is reported in Figure 9a. Fracture areas are in the range of 0.35 and 0.78 m^2, and the six fracture intersection lengths are in the interval of 0.48-0.65 m. Consequently, even if the number of fractures coincides with the one used in Test 2, this problem is characterized by a higher geometric complexity. Two globally conforming meshes are used and reported in Figure 9: a mesh consisting of 6326 elements (11746 nodes) constructed from six different locally conforming meshes made of non-uniform polygons (Figure 9a) and a mesh consisting of 6700 elements (3834 nodes) constructed from six different locally conforming meshes made of triangles (Figure 9b). The test performed on the latter mesh can be considered comparable to a classic Finite Element simulation, since the resulting number of non-triangular mesh cells is around 10% after the generation of the globally conforming mesh.

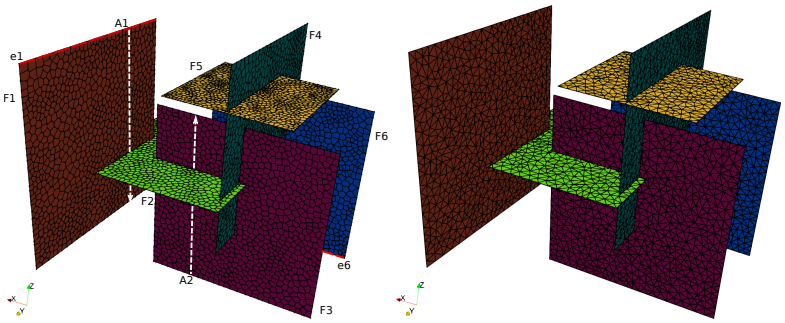

(a) (b)

Figure 9: Test 3: spatial distribution of fractures and two examples of globally conforming meshes for the 6-fracture DFN; each colour denotes a different fracture index i.

The DFN domain Ω is initially completely filled by the non-wetting phase fluid; consequently, we set $S_w = 0\ [-],\ x \in \Omega, t = 0\ [s]$ as initial condition for the saturation of the wetting phase. Moreover, we consider the following boundary conditions: we set constant Dirichlet boundary conditions $p_n = 2 \cdot 10^5\ [Pa]$ and $S_w = 0.8\ [-]$ on the top edge of F_1 (edge e_1) and a homogeneous Dirichlet boundary condition $S_w = 0\ [-]$ and a Neumann boundary condition $\boldsymbol{u} \cdot \boldsymbol{n}_\Omega = 0\ [m \cdot s^{-1}]$ on the bottom edge of F_6 (edge e_6), see Figure 9a. On all the remaining edges of the DFN we prescribe homogeneous Neumann boundary conditions $\boldsymbol{u} \cdot \boldsymbol{n}_\Omega = 0\ [m \cdot s^{-1}]$ and $\boldsymbol{u}_w \cdot \boldsymbol{n}_\Omega = 0\ [m \cdot s^{-1}]$, denoting by $\boldsymbol{n}_\Omega$ the unit normal pointing outward associated with the boundary of the domain Ω. Moreover, we set $q = q_w = 0\ [s^{-1}]$ as in the model equations (9).

The porous medium and the fluids data used in the simulation are reported in Table 4; moreover, the gravity term is taken into account.

Porosity	$\Phi = 0.3\ [-]$
Absolute permeability	$K = 10^{-10}\ [m^2]$
Residual saturations	$S_{wr} = 0,\ S_{nr} = 0\ [-]$
Viscosities	$\mu_w = 0.001,\ \mu_n = 0.020\ [Pa \cdot s]$
Densities	$\rho_w = 5000,\ \rho_n = 200\ [Kg/m^3]$
Brooks-Corey parameters	$\mu = 2.0\ [-],\ p_d = 5000\ [Pa]$

Table 4: Test 3: porous medium and fluids data.

In order to speed up the bidirectional displacement process, we increase both the value of

the density of the wetting phase ρ_w and the value of the entry pressure p_d with respect to Test 2; moreover, we decrease the value of the density of the non-wetting phase ρ_n. Due to the gravity effect, this implies that in a relatively small time interval the saturation of the wetting phase achieves values close to one in some parts of the DFN domain. As in Test 2, the capillary pressure p_c is not neglected; consequently, the saturation equation has a parabolic nature, but degenerate parabolic. Indeed, similarly to what was explained in Subsection 5.3, the diffusive term tends to vanish when the saturation approaches either zero or one. While the saturation of the wetting phase close to zero seems to not affect too much the proposed numerical scheme, values close to one can generate instabilities that reduce the physical validity of the numerical solution. Indeed, when the saturation reaches one, instead of preserving this physical upper bound, it tends to further increase; furthermore, it can also exhibit an oscillatory behaviour. To cope with this unphysical behaviour and stabilize the method, we combined three different strategies. Firstly, we adopt a local correction on the numerical saturation; in particular, we set to 0.99 the values of the saturation that are greater than one on the quadrature nodes and that are employed in the quadrature formula used to numerical approximate the integrals. Secondly, we change the global solution provided by the Newton method setting to 0.99 the values above one. Thirdly, we add an artificial stabilization term proportional to the saturation of the wetting phase, namely

$$(\tilde{\beta}(S_{w_\delta})\ K_F\ \hat{\Pi}^0_{k_S-1}\hat{\nabla}S_{w_\delta}, \hat{\Pi}^0_{k_S-1}\hat{\nabla}v_{S_\delta}), \quad \tilde{\beta}(S_{w_\delta}) = \beta\ (\hat{\Pi}^0_{k_S}S_{w_\delta})^2, \tag{19}$$

with β a suitable selected constant. The dependency of the coefficient $\tilde{\beta}$ on the saturation implies that the artificial stabilization contributes more when the saturation is relatively close to one. This allows us to stabilize the numerical saturation solution only when it reaches values close to one without affecting the solution globally. We underline that we have decided to combined all the three strategies previously described because the results obtained applying them separately were unsatisfactory.

In the numerical simulation, we consider a time step $\Delta t = 5$ $[s]$ and a VEM order $k = 1$. In Figures 10-11, we report the saturation of the wetting phase and the pressure of the non-wetting phase at three different times. In the figures the colouring is proportional to the values of the saturation and of the pressure, respectively. Since edge e_1 is located in the upper part of the domain, edge e_6 is located in the lower part and the other edges are impervious (Figure 9a) the wetting phase fluid moves rapidly toward the bottom part of F_1 where it starts to accumulate (Figure 10b). Then, the wetting phase enters F_2 and so it reaches also F_3. Here it start to accumulate in the bottom part until it reaches the intersection with F_4. Finally, through F_4, the wetting phase fluid arrives in F_6 (Figure 10c). The wetting phase fluid does not enter F_5 that remains completely filled by the non-wetting phase fluid. As expected, we can observe that when the gravity acts in the same direction of the wetting phase fluid, it assists the imbibition of the wetting phase fluid.

In Figure 11, we notice that, at a fixed time instant, the pressure is constant along the horizontal fractures F_2 and F_5, whereas it is clearly not constant along the vertical fractures F_1 and F_3 (Figures 11b and 11c).

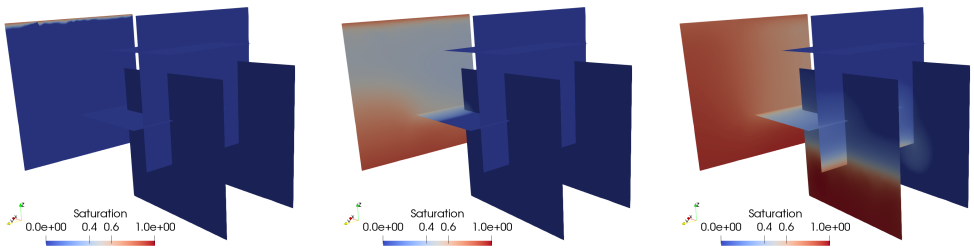

(a) $t = 0$ [s] $(g \neq 0)$ (b) $t = 701$ [s] $(g \neq 0)$ (c) $t = 5351$ [s] $(g \neq 0)$

Figure 10: Test 3: saturation of the wetting phase S_w $[-]$ at three different time instants, gravity activated $(g \neq 0)$ and VEM order $k = 1$.

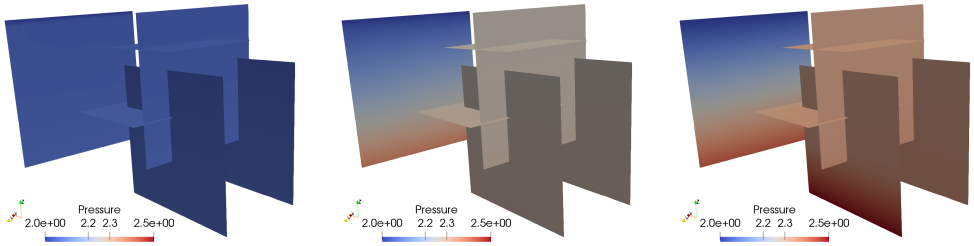

(a) $t = 0$ [s] ($g \neq 0$) (b) $t = 701$ [s] ($g \neq 0$) (c) $t = 5351$ [s] ($g \neq 0$)

Figure 11: Test 3: pressure of the non-wetting phase p_n [bar] at three different time instants, gravity activated ($g \neq 0$) and VEM order $k = 1$.

To better understand the behaviour of the saturation of the wetting phase when it reaches values close to one, we analyse the saturation profile along two vertical lines displayed in Figure 9a and denoted as A_1 and A_2, respectively. The results are reported in Figure 12 and in Figure 13 for A_1 and A_2, respectively.

Firstly, we focus on the mesh reported in Figure 9b and we analyse the case in which none of the stabilizing strategies described above is applied. When the saturation approaches one, it starts to exhibit strong oscillations and eventually it exceeds one. This behaviour is described by the black dotted line reported in Figure 12c. Therefore, to mitigate the unphysical behaviour of the solution, we adopt the three strategies previously described. In particular, we consider the behaviour of the solution for a value of the parameter $\beta = -0.2$. The related saturation profile along A_1 (Figure 12) and along A_2 (Figure 13) is described by the rounded blue continuous lines. Comparing Figures 12a-12c and Figures 13a-13c we can see that, as expected, the artificial stabilization term contributes more when the saturation is relatively close to one. Indeed, in the other cases, the black dotted and the rounded blue saturation profiles exhibit the same behaviour.

Finally, we apply the same stabilization strategies to the mesh reported in Figure 9a choosing the same value of the parameter β. The saturation profiles along A_1 (Figure 12) and A_2 (Figure 13) are described by the squared red continuous lines.

In Figure 12c, we can see that the three saturation profiles exhibit slightly different behaviours close to $s = 0.0$ and close to $s = 0.6$ where s is the curvilinear coordinate along A_1. Indeed, near those two regions of the domain the saturation solution is characterized by strong gradients. In the first case they are related to the discontinuity due to the fixed boundary condition on edge e_1, while in the second case they are related to jump due to the presence of the intersection between F_1 and F_2.

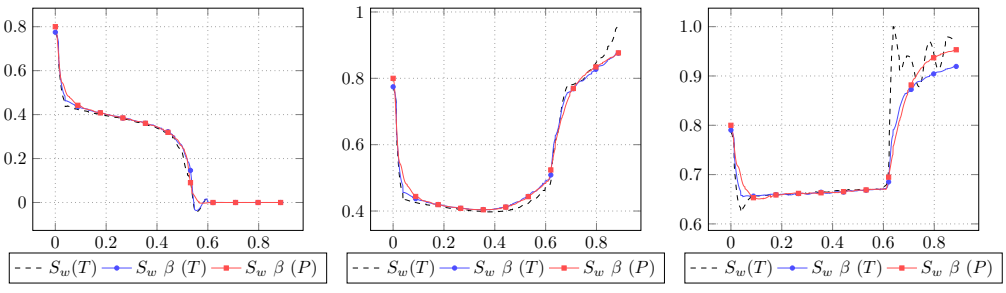

(a) S_w [-], $t = 201$ [s] (b) S_w [-], $t = 701$ [s] (c) S_w [-], $t = 1951$ [s]

Figure 12: Test 3: profile of the saturation of the wetting phase S_w [−] at three different time instants along A_1 (Figure 9a); Profiles are measured on the triangular mesh with no stabilization [(T)], on the triangular mesh with stabilization [$\beta\ (T)$] and on polygonal mesh with stabilization [$\beta\ (P)$].

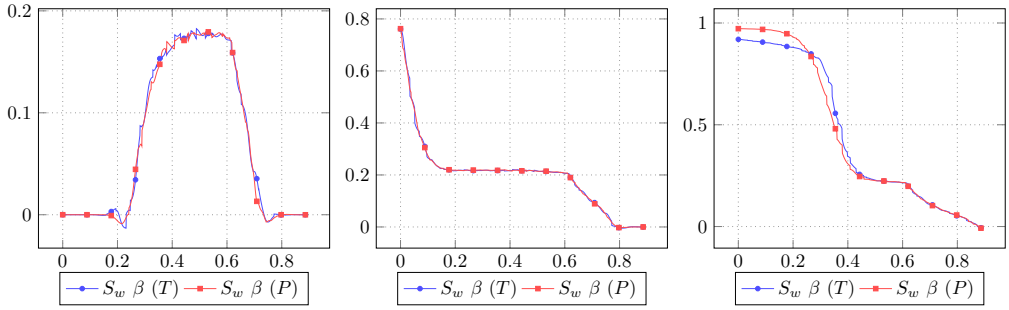

(a) S_w [-], $t = 1201$ [s] (b) S_w [-], $t = 1951$ [s] (c) S_w [-], $t = 4951$ [s]

Figure 13: Test 3: profile of the saturation of the wetting phase S_w $[-]$ at three different time instants along A_2 (Figure 9a); Profiles are measured on the triangular mesh with stabilization $[\beta\ (T)]$ and on polygonal mesh with stabilization $[\beta\ (P)]$.

In Figures 14 and 15, we show the pressure profiles related to the saturation profiles of Figures 12 and 13, respectively. We can observe that the variations on the saturation solution do not significantly impact on the pressure solution.

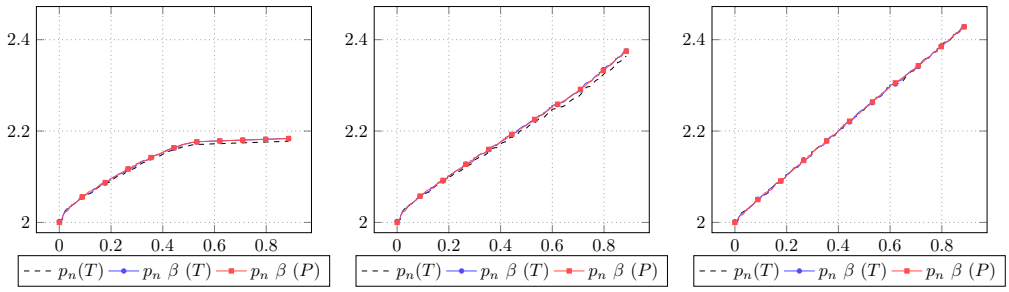

(a) p_n [bar], $t = 201$ [s] (b) p_n [bar], $t = 701$ [s] (c) p_n [bar], $t = 1951$ [s]

Figure 14: Test 3: pressure of the non-wetting phase p_n [bar] at three different time instants along A_1 (Figure 9a); Profiles are measured on the triangular mesh with no stabilization $[(T)]$, on the triangular mesh with stabilization $[\beta\ (T)]$ and on polygonal mesh with stabilization $[\beta\ (P)]$.

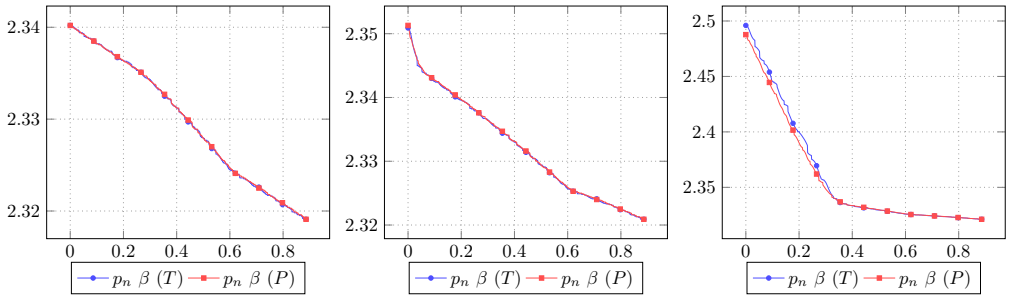

(a) p_n [bar], $t = 1201$ [s] (b) p_n [bar], $t = 1951$ [s] (c) p_n [bar], $t = 4951$ [s]

Figure 15: Test 3: pressure of the non-wetting phase p_n [bar] at three different time instants A_2 (Figure 9a); Profiles are measured on the triangular mesh with stabilization $[\beta\ (T)]$ and on polygonal mesh with stabilization $[\beta\ (P)]$.

5.5 Test 4: 20-fracture realistic DFN

In Test 4 we propose a validation of our approach simulating a counter-current imbibition problem on a complex DFN domain involving 20 rectangular fractures, each one of area ≈ 2 m^2. The spatial distribution of the fractures is shown in Figure 16 together with the globally conforming mesh consisting of 18140 elements (15054 nodes) and constructed from 20 locally conforming meshes made of triangles. We start from local triangular meshes on each domain since they are more frequently encountered in engineering applications. However, we point out that, due to the high complexity of the network (see Figure 16), the final global conforming mesh counts almost 70% of non-triangular cells, making the VEM approach proposed necessarily. The selected DFN structure shows complexities typically present in problems of interest for practical applications; in particular, it involves an intricate network of fractures that intersect each other giving rise to very narrow angles (see Figure 16b). In Figure 17 and Table 5 we report some statistics on the network and mesh data. In Figure 17 the lengths [m] distribution of the 182 fracture intersections of the network is presented ordered from the smallest to the largest length; from the plot we can see that the DFN structure presents a wide range of random intersections from 0.1 to 2.0 meters. In Table 5 we report the statistic data on the mesh edge lengths $|e|$ [m], the mesh cells areas $|E|$ [m^2] and the mesh cell aspect ratios η, defined for each mesh cell E as the ratio between the radius of the circumscribed and inscribed polygon circumference. From the minimum and maximum area values we can see that elements as small as 10^{-13} m^2 are present in the global conforming mesh together with elements ten orders larger in magnitude; moreover, from the aspect ratio data we can observe that distorted elements are present as well, as the ones highlighted in Figure 16b.

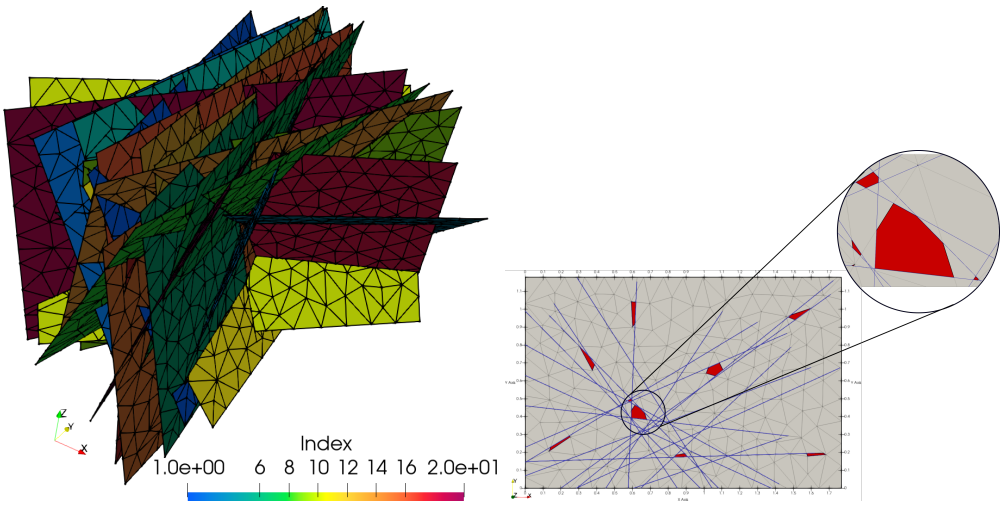

(a) Spatial DFN distribution with globally conforming mesh; each colour denotes a different fracture index i.

(b) Fracture $i = 5$ rotated in its tangential system. Fracture intersections are reported (blue segments) and some bad shapes elements are enlighted (red cells).

Figure 16: Test 4: DFN with 20 fractures.

We consider the same parameters of the porous medium and the same fluids data reported in Table 4 for Test 3 expect for the densities ($\rho_w = 1000$, $\rho_n = 400$ $[Kg/m^3]$) and the same initial and boundary conditions described in Test 3. In particular, we set constant Dirichlet boundary conditions $p_n = 2 \cdot 10^5$ $[Pa]$ and $S_w = 0.8$ $[-]$ on the upper part of the domain (edge e_i) and homogeneous Dirichlet boundary condition $S_w = 0$ $[-]$ and homogeneous Neumann boundary condition $\boldsymbol{u} \cdot \boldsymbol{n}_\Omega = 0$ $[m \cdot s^{-1}]$ in the lower part of the domain (edge e_f), $t \in \mathcal{I}_T$, see Figure 18. Moreover, we set $q = q_w = 0$ $[s^{-1}]$ and we consider both a case in which the gravity is neglected and a case in which it is activated. We set a time step $\Delta t = 10$ $[s]$ and a VEM order $k = 1$.

In Figures 19-20 we show the numerical solution for the saturation of the wetting phase for three different time instants. In the figures the colouring is proportional to the values of the

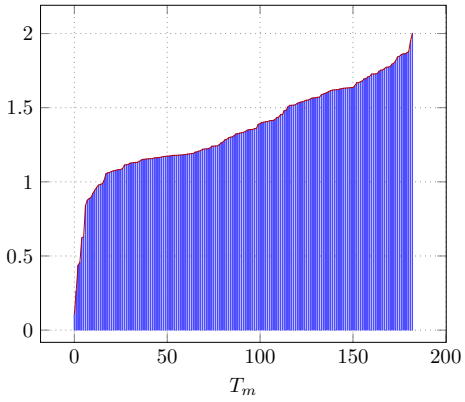

Figure 17: Test 4: fracture intersection length [m] distribution ordered from the smallest to the largest length.

	min	max	avg
$\|e\|$	6.10E-07	2.03E-01	4.15E-02
$\|E\|$	7.16E-13	9.95E-03	2.31E-03
η	1.49E+00	1.37E+02	4.64E+00

Table 5: Test 4: minimum, maximum and average mesh edge length ($|e|$), mesh cell area ($|E|$) and mesh cell aspect ratio (η) are reported.

saturation. In particular, Figure 20 displays the solutions in case the gravity is considered for the back of the DFN domain; whereas, Figure 19 displays the solutions in case the gravity is neglected. We can observe that if the gravity is not activated what matters most is the connection among the fractures in the network rather than their location. Indeed, at the beginning the wetting fluid tends to spread throughout the network and only later it starts to accumulate. We can also observe the complexity of the resulting globally conforming mesh that turns out to be challenging. The qualitative analysis of the solutions shows that the proposed approach is capable of handling these types of meshes producing reliable physical solutions.

In Figures 22-21 we report the numerical solution for the pressure of the non-wetting phase for three different time instants. In the figures the colouring is proportional to the values of the pressure. Figure 22 displays the solution in case the gravity is considered; on the other hand, Figure 21 displays the solution in case the gravity is neglected. In case gravity is activated the pressure achieves higher values.

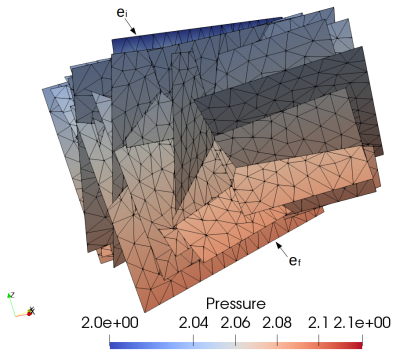

(a) Pressure of the non-wetting phase p_n [bar] (Front)

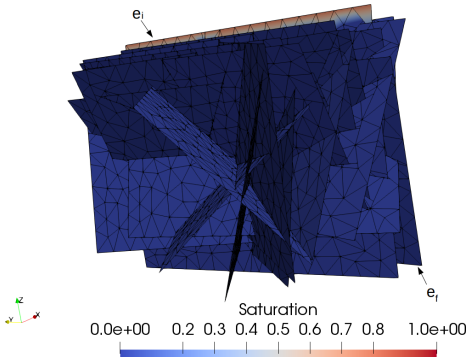

(b) Saturation of the wetting phase S_w [−] (Back)

Figure 18: Test 4: Initial condition at $t = 0$ $[s]$ and VEM order $k = 1$.

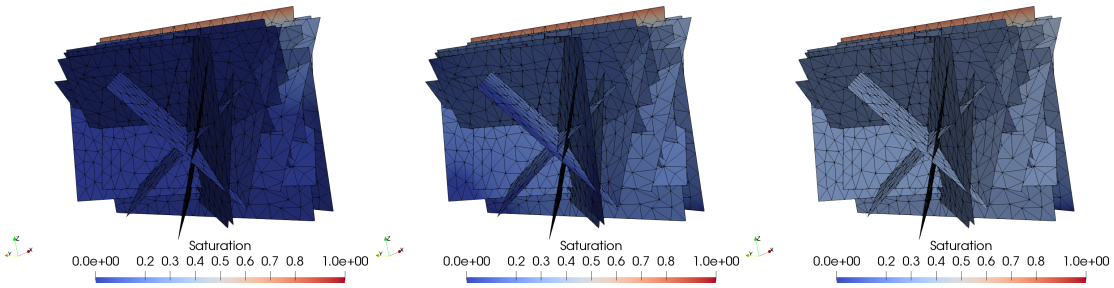

(a) $t = 2301$ [s] (b) $t = 12301$ [s] (c) $t = 21401$ [s]

Figure 19: Test 4: saturation of the wetting phase S_w [−] at three different time instants in case gravity is neglected ($g = 0$) and VEM order $k = 1$ (Back).

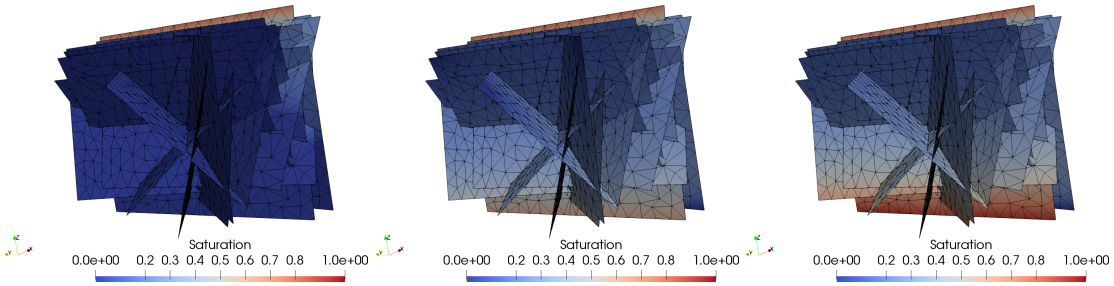

(a) $t = 2301$ [s] (b) $t = 12301$ [s] (c) $t = 21401$ [s]

Figure 20: Test 4: saturation of the wetting phase S_w [−] at three different time instants in case gravity is activated ($g \neq 0$) and VEM order $k = 1$ (Back).

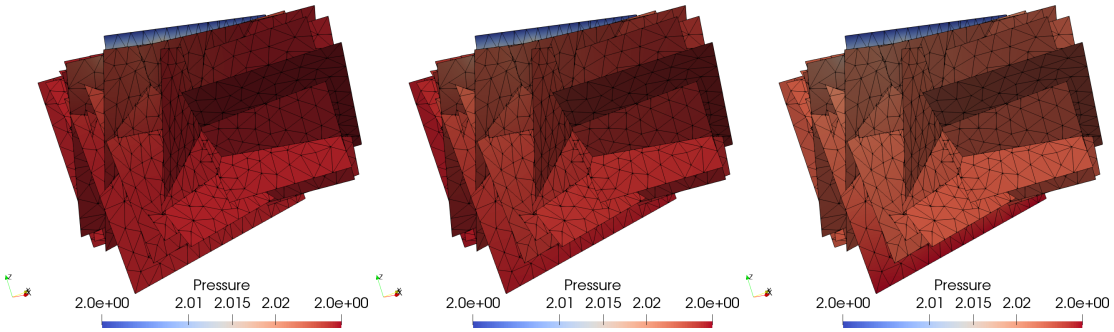

(a) $t = 2301$ [s] (b) $t = 12301$ [s] (c) $t = 21401$ [s]

Figure 21: Test 4: pressure of the non-wetting phase p_n at three different time instants in case gravity is neglected ($g = 0$) and VEM order $k = 1$ (Front).

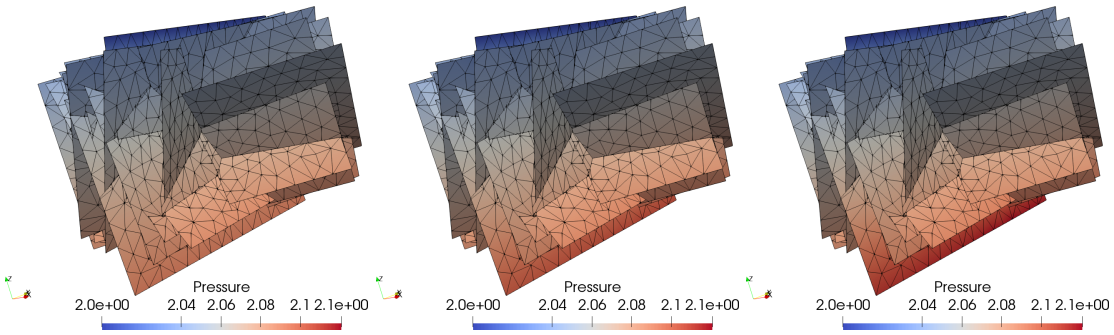

(a) $t = 2301$ [s] (b) $t = 12301$ [s] (c) $t = 21401$ [s]

Figure 22: Test 4: pressure of the non-wetting phase p_n $[bar]$ at three different time instants in case gravity is activated ($g \neq 0$) and VEM order $k = 1$ (Front).

6 Conclusion

In this work we have proposed a virtual element approach to the simulation of two-phase flow of immiscible fluids in poro-fractured media. The fractured media has been modelled via a Discrete Fracture Network. With respect to the classical DFN model, we have further assumed that all the fractures are characterized by the same isotropic rock type and the same width. This guarantees the continuity of the saturation of the wetting phase on the traces. The proposed method has been tested on different DFN models of increasing complexity from a simple two-fracture network having known analytical solution to a more complex and realistic twenty-fracture network characterized by challenging features. The numerical results reported prove the robustness of the approach with respect to the geometrical complexity of the underlying grid. A local artificial stabilization term is introduced to manage extreme situations for the saturation of the wetting phase.

Acknowledgments

We acknowledge the support of the computational resources partially provided by HPC@PoliTO and Smart-Data@PoliTO. This work was partially supported by the MIUR project "Dipartimenti di Eccellenza 2018-2022" (grant number E11G18000350001); the PRIN Project "Virtual Element Methods: Analysis and Applications" (project number 201744KLJL_004); the PRIN Project 0204LN5N5_003 and INdAM-GNCS (Italy).

References

[1] P. M. Adler, J.-F. Thovert, Fractures and fracture networks, Vol. 15, Springer Science & Business Media, 1999.

[2] P. Dietrich, R. Helmig, H. Hötzl, M. Sauter, J. Köngeter, G. Teutsch, Flow and transport in fractured porous media, Springer Science & Business Media, 2005.

[3] P. M. Adler, J.-F. Thovert, V. V. Mourzenko, Fractured porous media, Oxford University Press, 2013.

[4] A. Fumagalli, I. Berre, Numerical methods for processes in fractured porous media, Birkhäuser, 2019.

[5] D. Qi, T. Hesketh, An analysis of upscaling techniques for reservoir simulation, Petroleum science and technology 23 (7-8) (2005) 827–842.

[6] M.-C. Cacas, E. Ledoux, G. de Marsily, B. Tillie, A. Barbreau, E. Durand, B. Feuga, P. Peaudecerf, Modeling fracture flow with a stochastic discrete fracture network: calibration and validation: 1. the flow model, Water Resources Research 26 (3) (1990) 479–489.

[7] V. Martin, J. Jaffré, J. E. Roberts, Modeling fractures and barriers as interfaces for flow in porous media, SIAM Journal on Scientific Computing 26 (5) (2005) 1667–1691.

[8] J. D. Hyman, S. Karra, N. Makedonska, C. W. Gable, S. L. Painter, H. S. Viswanathan, dfnworks: A discrete fracture network framework for modeling subsurface flow and transport, Computers & Geosciences 84 (2015) 10–19.

[9] T. D. Ngo, A. Fourno, B. Noetinger, Modeling of transport processes through large-scale discrete fracture networks using conforming meshes and open-source software, Journal of Hydrology 554 (2017) 66–79.

[10] C. Xu, C. Fidelibus, P. Dowd, Z. Wang, Z. Tian, An iterative procedure for the simulation of the steady-state fluid flow in rock fracture networks, Engineering Geology 242 (2018) 160–168. doi:https://doi.org/10.1016/j.enggeo.2018.06.005.
URL https://www.sciencedirect.com/science/article/pii/S0013795217318033

[11] S. Berrone, S. Pieraccini, S. Scialò, A pde-constrained optimization formulation for discrete fracture network flows, SIAM Journal on Scientific Computing 35 (2) (2013) B487–B510. doi:10.1137/120865884.
URL https://doi.org/10.1137/120865884

[12] S. Berrone, S. Pieraccini, S. Scialò, On simulations of discrete fracture network flows with an optimization-based extended finite element method, SIAM Journal on Scientific Computing 35 (2) (2013) A908–A935. doi:10.1137/120882883.
URL https://doi.org/10.1137/120882883

[13] S. Berrone, A. D'Auria, S. Scialo, An optimization approach for flow simulations in poro-fractured media with complex geometries, Computational Geosciences 25 (3) (2021) 897–910.

[14] S. Berrone, D. Grappein, S. Pieraccini, S. Scialó, A three-field based optimization formulation for flow simulations in networks of fractures on nonconforming meshes, SIAM Journal on Scientific Computing 43 (2) (2021) B381–B404.

[15] S. Berrone, S. Pieraccini, S. Scialò, An optimization approach for large scale simulations of discrete fracture network flows, Journal of Computational Physics 256 (2014) 838–853. doi:https://doi.org/10.1016/j.jcp.2013.09.028.
URL https://www.sciencedirect.com/science/article/pii/S0021999113006426

[16] F. Chave, D. A. Di Pietro, L. Formaggia, A hybrid high-order method for darcy flows in fractured porous media, SIAM Journal on Scientific Computing 40 (2) (2018) A1063–A1094.

[17] P. F. Antonietti, L. Formaggia, A. Scotti, M. Verani, N. Verzott, Mimetic finite difference approximation of flows in fractured porous media, ESAIM: Mathematical Modelling and Numerical Analysis 50 (3) (2016) 809–832.

[18] A. Fumagalli, E. Keilegavlen, Dual virtual element method for discrete fractures networks, SIAM Journal on Scientific Computing 40 (1) (2018) B228–B258.

[19] M. F. Benedetto, S. Berrone, S. Scialò, A globally conforming method for solving flow in discrete fracture networks using the virtual element method, Finite Elements in Analysis and Design 109 (2016) 23–36.

[20] M. F. Benedetto, S. Berrone, S. Pieraccini, S. Scialò, The virtual element method for discrete fracture network simulations, Computer Methods in Applied Mechanics and Engineering 280 (2014) 135–156. doi:https://doi.org/10.1016/j.cma.2014.07.016.
URL https://www.sciencedirect.com/science/article/pii/S0045782514002485

[21] M. F. Benedetto, A. Borio, F. Kyburg, J. Mollica, S. Scialò, An arbitrary order mixed virtual element formulation for coupled multi-dimensional flow problems, Computer Methods in Applied Mechanics and Engineering 391 (2022) 114204.

[22] S. Berrone, S. Pieraccini, S. Scialo, F. Vicini, A parallel solver for large scale dfn flow simulations, SIAM Journal on Scientific Computing 37 (3) (2015) C285–C306.

[23] G. Pichot, P. Laug, J. Erhel, R. Le Goc, C. Darcel, P. Davy, J.-R. de Dreuzy, Simulations in large tridimensional discrete fracture networks (dfn): Ii. flow simulations, in: MASCOT 2018-15th IMACS/ISGG meeting on applied scientific computing and tools, 2018.

[24] S. Berrone, A. Borio, C. Fidelibus, S. Pieraccini, S. Scialò, F. Vicini, Advanced computation of steady-state fluid flow in discrete fracture-matrix models: Fem–bem and vem–vem fracture-block coupling, GEM - International Journal on Geomathematics 9 (2) (2018) 377–399. doi:10.1007/s13137-018-0105-3.
URL https://doi.org/10.1007/s13137-018-0105-3

[25] R. Helmig, et al., Multiphase flow and transport processes in the subsurface: a contribution to the modeling of hydrosystems., Springer-Verlag, 1997.

[26] Z. Chen, G. Huan, Y. Ma, Computational methods for multiphase flows in porous media, SIAM, 2006.

[27] H. Hoteit, A. Firoozabadi, An efficient numerical model for incompressible two-phase flow in fractured media, Advances in Water Resources 31 (6) (2008) 891–905.

[28] J. Jaffré, M. Mnejja, J. E. Roberts, A discrete fracture model for two-phase flow with matrix-fracture interaction, Procedia Computer Science 4 (2011) 967–973.

[29] D. Gläser, R. Helmig, B. Flemisch, H. Class, A discrete fracture model for two-phase flow in fractured porous media, Advances in Water Resources 110 (2017) 335–348.

[30] A. Fumagalli, A. Scotti, A numerical method for two-phase flow in fractured porous media with non-matching grids, Advances in Water Resources 62 (2013) 454–464.

[31] S. Berrone, M. Busetto, A virtual element method for the two-phase flow of immiscible fluids in porous media, Computational Geosciences (2022) 1–22.

[32] E. Ahmed, J. Jaffré, J. E. Roberts, A reduced fracture model for two-phase flow with different rock types, Mathematics and Computers in Simulation 137 (2017) 49–70.

[33] R. H. Brooks, Hydraulic properties of porous media, Colorado State University, 1965.

[34] P. Bastian, Numerical Computation of Multiphase Flow in Porous Media, Ph.D. thesis, Christian-Albrechts-Universität Kiel (1999).

[35] L. Beirão da Veiga, F. Brezzi, L. D. Marini, A. Russo, Virtual element method for general second-order elliptic problems on polygonal meshes, Mathematical Models and Methods in Applied Sciences 26 (04) (2016) 729–750.

[36] A. Cangiani, G. Manzini, O. J. Sutton, Conforming and nonconforming virtual element methods for elliptic problems, IMA Journal of Numerical Analysis 37 (3) (2017) 1317–1354.

[37] J. R. Shewchuk, Triangle: Engineering a 2d quality mesh generator and delaunay triangulator, in: Workshop on Applied Computational Geometry, Springer, 1996, pp. 203–222.

[38] C. Talischi, G. H. Paulino, A. Pereira, I. F. Menezes, Polymesher: a general-purpose mesh generator for polygonal elements written in matlab, Structural and Multidisciplinary Optimization 45 (3) (2012) 309–328.

[39] D. B. McWhorter, D. K. Sunada, Exact integral solutions for two-phase flow, Water Resources Research 26 (3) (1990) 399–413.

[40] P. Bastian, Numerical computation of multiphase flows in porous media, Ph.D. thesis, habilitationsschrift Univeristät Kiel (1999).

[41] T. I. Bjørnarå, S. A. Mathias, A pseudospectral approach to the mcwhorter and sunada equation for two-phase flow in porous media with capillary pressure, Computational Geosciences 17 (6) (2013) 889–897.

[42] M. El-Amin, A. Salama, S. Sun, Effects of gravity and inlet location on a two-phase countercurrent imbibition in porous media, International Journal of Chemical Engineering 2012.

[43] S. Li, Y.-h. Ding, B. Cai, Y. Lu, D. Gu, Solution for counter-current imbibition of 1d immiscible two-phase flow in tight oil reservoir, Journal of Petroleum Exploration and Production Technology 7 (3) (2017) 727–733.